Master's thesis

2019

Michiel Desmedt

NTNU
Norwegian University of Science and Technology
Faculty of Information Technology and Electrical Engineering
Department of Electric Power Engineering

Michiel Desmedt

Dynamical electromechanical analysis of pole-piece rotors in pseudo direct-drive machines

Taking the next step towards tomorrow's wind turbines

December 2019

NTNU
Norwegian University of
Science and Technology

NTNU
Norwegian University of
Science and Technology

NTNU

Norwegian University of
Science and Technology

Dynamical electromechanical analysis of pole-piece rotors in pseudo direct-drive machines

Taking the next step towards tomorrow's wind turbines

Michiel Desmedt

European Wind Energy Master
Submission date: December 2019
Supervisor: Robert Nilssen
Co-supervisor: Jianning Dong

Norwegian University of Science and Technology
Department of Electric Power Engineering

Dynamical electromechanical analysis of pole-piece rotors in pseudo direct-drive machines

by

Michiel Desmedt

in fulfillment of the requirements for the degrees of
MSc in Electrical Engineering at Delft University of Technology
&
MSc-Technology in Wind Energy at Norwegian University of Science and Technology,
under the European Wind Energy Masters programme.

To be defended publicly
on Friday December 6, 2019 at TU Delft.

Supervisor:	Dr. ir. J. Dong,	TU Delft
Thesis committee:	Prof. Dr. ir. P. Bauer,	TU Delft
	Dr. ir. J. Dong,	TU Delft
	Prof. R. Nilssen,	NTNU

Preface

This report is written as a master thesis concluding my European Wind Energy Master. The purpose of this thesis is threefold: first of all, it has a scientific value by doing research on a topic which has never been investigated before. This will be elaborately described in this report. The second goal is to prove the readiness to receive the degree of Master in Science by displaying the skills gathered throughout the last couple of years.

The third goal, while perhaps being the most important one, cannot be described in words. Spending time on the same topic for almost a year, the late nights, struggling with problems and the patience required to solve them definitely have left their mark on me and allowed me to grow on a personal level taking courses just cannot provide.

This would not have been possible without the support of my supervisors. I want to specifically express my gratitude towards my daily supervisor, Jianning Dong, for guiding me during my thesis, and showing his understanding during the though times I encountered during the thesis project. I would also like to thank Pavol Bauer and Robert Nilssen for being in my thesis committee. Additionally, I would like to thank Henk Polinder who has, directly and indirectly, guided me on an academic as well as a personal level during the last couple of years.

I would also like to thank my family, and more specifically my parents for supporting me, year after year, emotionally and financially. Without them, I would not even have had the opportunity to be where I am now. I am eternally grateful for that.

Having the opportunity is one thing, but keeping up with all the work would not be possible without spending time with friends once in a while. I would like to thank all the people I met in the last couple of years for that, but I am especially grateful to my close friends without whom my years at university would not have been as fun as they have been.

And last but definitely not least, I would like to thank my girlfriend Sara for her continuous support when times got tough, endless patience when I was complaining about my thesis, and her never ending effort to keep me sane when I broke my COMSOL models once again.

Michiel Desmedt

Delft, December 2019

Table of Contents

List of Figures

Chapter 1

Introduction

In this chapter, the motivation behind this research will be discussed, as well as the existing research already done on the same topic. The scientific gap will be identified, followed by the statement of the research question. Finally, the outline of the thesis will be discussed.

1.1 Background

With the effects of climate change being increasingly visible, more attention is going to setting ambitious targets to curb global warming, with the long-term goal of limiting the temperature rise to 2 degrees Celsius [1]. With targets set for 2020, Europe had clear targets and a roadmap for the next decade, of which one target is to increase the share of renewable energy sources to 20 % [2]. In the following decade, Europe was set to reach the target, but the recent increase in primary energy consumption halted the growth, which means more efforts need to be done in order to reach the 2020 targets [3].

With the 2020 deadline near, Europe has already set targets for 2030 as well, as part of the roadmap to limit global warming, which includes increasing the share of renewable energy sources further to 32 % [3]. This means Europe needs to step up its efforts, emphasized by the European Commission, who called the drafts of the National Energy and Climate Plans of the EU member states insufficient to deliver on the EU's 2030 energy targets [4].

Wind power has shown great potential, delivering an increasing number of wind power plants in the recent years [4–6], making big strides to the 2030 targets. A graph of the yearly installed wind power capacity of the last 7 years and a projection of the next 4 years can be seen in Figure 1.1. However, the development of offshore wind parks can take up to ten years. Therefore, it is important to already push new technological advances, as the technology of today will result in the wind turbines of the next decade [4].

One of the reasons why wind is becoming increasingly popular, is the decrease in LCOE [7–10], as seen in Figure 1.2. However, to further incentivize and increase its competitiveness with non-renewable energy sources, the LCOE should be decreased even further. This is why

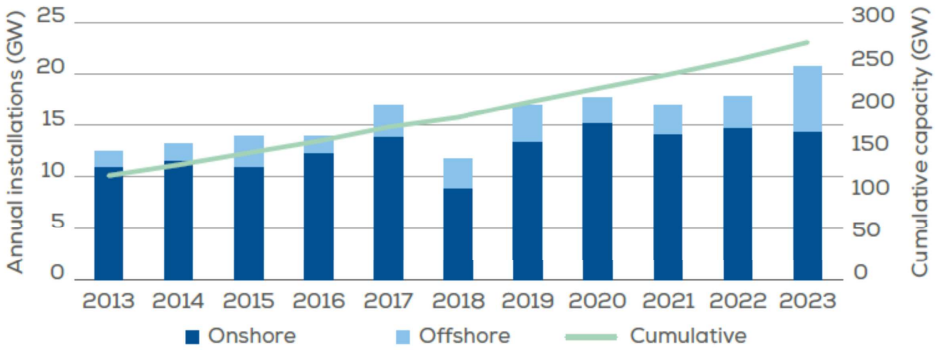

Figure 1.1: Yearly installed wind power capacity, including a projection up to 2023 [4]

projects such as INNWIND were started, focusing on decreasing the LCOE, specifically aimed at larger $10 - 20$ MW wind turbines [11]. Increasing the size of single turbines has shown to decrease the LCOE significantly by increasing the capacity factor, and decreasing the BoP CAPEX (Balance-of-Plant Capital Expenditures), OPEX (Operational Expenditures) and DECEX (Decommissioning Expenditures) [12]. This is a result of the decreasing number of turbines compared to a farm of the same capacity consisting of smaller turbines. Especially offshore farms benefit from this, as maintenance is more expensive there, resulting in a clear trend showing the increasing size of offshore wind turbines [4].

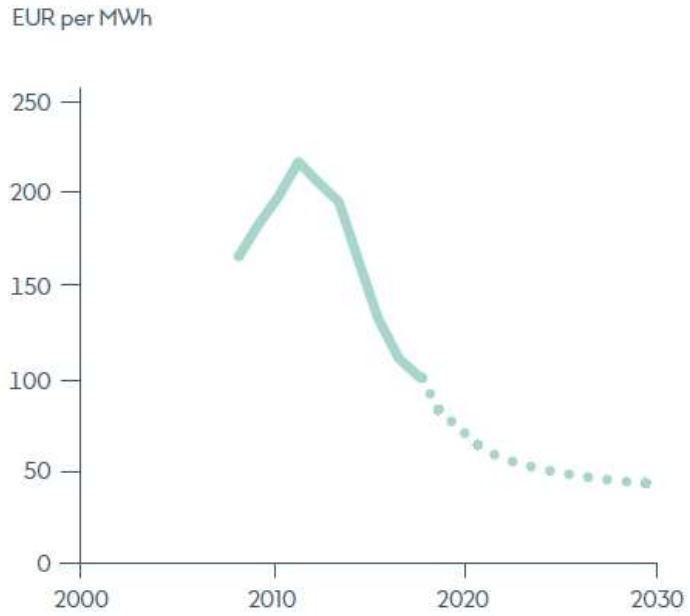

Figure 1.2: Yearly LCOE of offshore wind energy, including a projection up to 2030 [8]

Making offshore wind turbines more reliable and thus reducing maintenance is of prime importance when trying to reduce the LCOE. This is why most of the offshore wind turbines nowadays use direct-drive generators instead of geared generators, as the gear is shown to be a high-risk component in the drivetrain of a wind turbine [13–15]. Due to the slow rotational speed of the rotor however, the generator has to provide a high torque, requiring a large diam-

eter machine. With increasing size and mass, it becomes impractical to transport and install them, especially offshore. Next to that, the mass of a direct-drive permanent magnet machine is not linear with its rated power [16]. A simple way to see this is that the rated power of a wind turbine is quadratically proportional to the turbine rotor diameter. However, due to aerodynamic and structural limitations, the rotational speed is inversely proportional to the turbine rotor radius. This means that the torque to be provided to increase the generator power is scaling non-linearly with rated power. Since the volume of a generator rotor is at best linearly proportional to the torque, the mass will scale non-linearly as well.

In order to keep the generator compact, the speed of the rotor should be increased in order to make use of a more compact, lower torque generator. Instead of using a mechanical gearbox which is prone to wear due to the meshing teeth, it is possible to get rid of the meshing by transmitting the forces contactless. This is the working principle of magnetic gears [17–20]. These kind of gearboxes have several advantages, such as:

- **Less acoustic noise due to meshing teeth**. Since the teeth of a mechanical gear mesh in and out of each other at a high speed and frequency, they can induce audible noise which can cause discomfort for people in the vicinity.
- **No wearing down of the load-transmitting parts**. Also because of the meshing, the teeth may slowly wear down over time, reducing the power transmission efficiency or initiating crack which may even cause teeth to break off, damaging other gears and making the gearbox unusable.
- **Inherent overload protection**. Since there is no physical contact between parts of the magnetic gears, they cannot be damaged in case of a sudden overload on one of the rotors. Instead, the gears can just slip and re-engage when the overload has disappeared.

Using this kind of gearbox, most disadvantages of mechanical gearboxes are bypassed, and more compact generators can be used. Research has been done on integrating the machine into the magnetic gear volume, which are subsequently called pseudo direct-drive (PDD) machines [18, 21–23]. Due to the high torque density, it has shown to have some potential for future wind turbines [11, 24, 25]. After the feasibility of using PDD generators in wind turbines was proven [11], research moved from conceptual designing to analytical modelling [26, 27]. This research made optimisation easier and faster compared to more accurate yet slower numerical methods, which allowed more detailed research.

Because it is a part not seen in any other machine topologies, one of the more complex subjects of research of PDD machines is the pole-piece rotor, which is used to modulate the magnetic fields between the stator and the high-speed rotor. This pole-piece rotor ideally consists of an array of high-permeability steel beams magnetically isolated from each other. Research has been done on different pole-piece rotor designs [28, 29], focusing on magnetic performance and manufacturability, not mechanical behaviour. At the same time, research was also done focusing on the static mechanical optimisation of magnetic gears on MW-scale [30, 31]. This research has also focused on analytical modelling of the air gap flux density, but applying it to magneto-mechanical and thermal analysis [32].

Up until now, no research has been done on the dynamical mechanical behaviour of the pole-piece rotor. While this subject has already been investigated thoroughly in other machine topologies [33–37], it has not been investigated in PDD machines yet. Combining the

research on mechanical deformation of the pole-piece rotor with the vibrational analysis of other machine topologies makes an interesting area of research, as the electromagnetic force might interact with the resonance frequencies of the pole-pieces. This would cause problems such as the pole-pieces touching the magnet arrays and by doing that, causing wear and demagnetisation.

1.2 Problem Statement and Scope of Thesis

The main research question of this report is:

"What is the impact of modulating the air-gap flux distributions on the dynamic electromechanical behaviour of pole-piece rotors in pseudo direct-drive generators?"

The research takes the INNWIND design as a starting point [31]. It will be verified whether the proposed design, which has been optimised from an electro-mechanical point of view, also functions properly from a mechanical point of view. Next to quantifying the electromechanical behaviour of the pole-pieces, attention will be paid to improving the behaviour, resulting in the following research question:

"What modifications to the existing INNWIND design can improve the electromechanical behaviour of pole-piece rotors?"

Again, taking the INNWIND design as a starting point, the model will be modified with the aim of improving the electromechanical behaviour of the pole-pieces. This will be done by numerical means provided by the COMSOL Multiphysics software. It is chosen to work with a numerical tool rather than an analytical one due to its flexibility and robustness when applying changes to the model.

1.3 Thesis Structure

The report will start off with an introduction to PDD machines in Chapter 2, where a short overview of the history and working principle of PDD machines will be given, followed by a short introduction of the INNWIND project, the base for this report. In Chapter 3, the mathematical tools will be discussed, as well as the used work flow in COMSOL Multiphysics, including simulation settings. The building of the model itself will be discussed in Chapter 4, defining the scope and limits of the model before elaborating on how the electromagnetic and mechanical model were built and verified. The chapter ends with results of the INNWIND design. Then, model modifications will be presented and their results quantified and compared in Chapter 5 before concluding the report with the conclusions, scientific contributions and recommendations in Chapter 6.

Chapter 2

Introduction to Pseudo Direct-drive Machines

In order to introduce the technology and the machine being investigated in this report, this chapter will cover a short history and an explanation of the working principle of the PDD machine, before introducing the INNWIND project, which introduced the design which is under investigation in this report.

2.1 History

The history of magnetic gears, and thus PDD machines, reaches back to the start of last century, but it did not become popular until the start of this century, when the first high-performance designs were published. This increase in popularity can easily be seen in Figure 2.1. In this section, a short review will be given of the history of PDD machines. Such a review not only helps with the understanding of the working principle of this machine topology, explained in the next section, but also increases the appreciation for the development steps the technology has gone through throughout the last century.

The first mention of power transmission through magnetic forces can be traced back to 1901, when Armstrong filed a patent for a magnetic spur gear [38]. Here, instead of the teeth physically meshing, the teeth would attract each other due to magnetic forces created by coils wound around the teeth of one of the gears, as can be seen in Figure 2.2.

While this certainly was the first step towards modern magnetic gear technology, the magnetic spur gear topology did not achieve torque densities anywhere close to their mechanical counterpart [18]. Next to that, the excitation of the coils also caused resistive losses similar to the mechanical counterpart experiencing friction losses, not necessarily improving on the efficiency of mechanical gears during operation. In 1941, a patent was filed by Faus for a magnetic spur gear and worm gear, this time exchanging the coils for permanent magnets [39]. However, the properties of state-of-the-art AlNiCo-alloys being developed around that

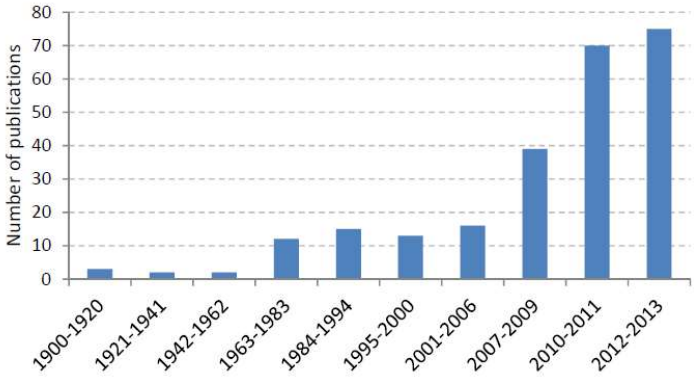

Figure 2.1: Graph showing the number of publications mentioning magnetic gears [18]

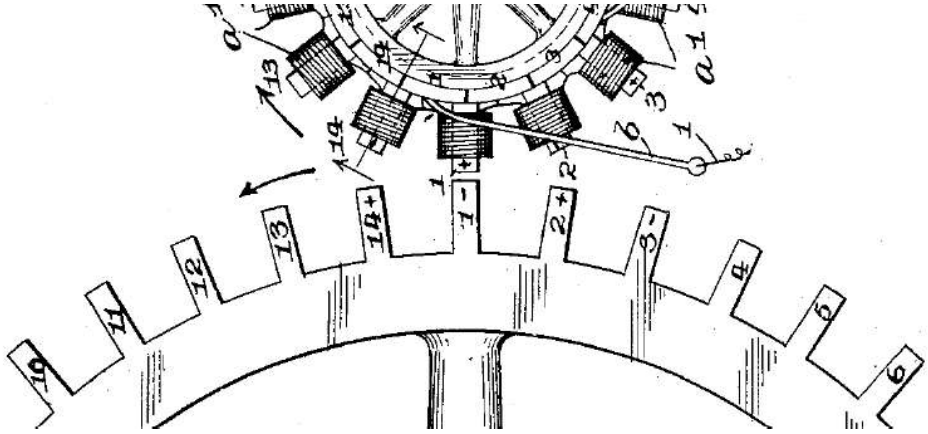

Figure 2.2: Close-up of the patent showing the first magnetic gear [38]

time were still far away from what current permanent material can achieve [40–42]. Next to that, the spur gear topology still did not make efficient use of the magnetic material, still having only a few magnets at a time engaging in power transmission.

In 1968, a breakthrough in magnetic gear technology happened when Martin filed a patent where the magnetic gear consists of three parts: two rotating bodies magnetically connected with each other through a third part, consisting of ferromagnetic material, called pole-pieces, as can be seen in Figure 2.3 [43]. By doing this, more magnetic material is engaged in transmitting power at the same time. The principle of modulating magnetic fields in order to link the fields of both moving parts is described in this patent as well, although not mathematically.

While different pole-piece shapes were tried out after the 1968 patent [44], most research narrowed down on rectangular or trapezoidal shaped pole-pieces. In the meantime, partly powered by technological advancements in magnet material, magnetic couplers got more interest, with the first mathematical analyses being published in 1978 [45]. However, it was not until 2001 that a high-performance magnetic gear was proposed by Atallah where a quantitative analysis was done with the help of numerical tools [46]. Mathematical analysis of this design was done by Atallah later as well [47], introducing the first principles of designing magnetic gears.

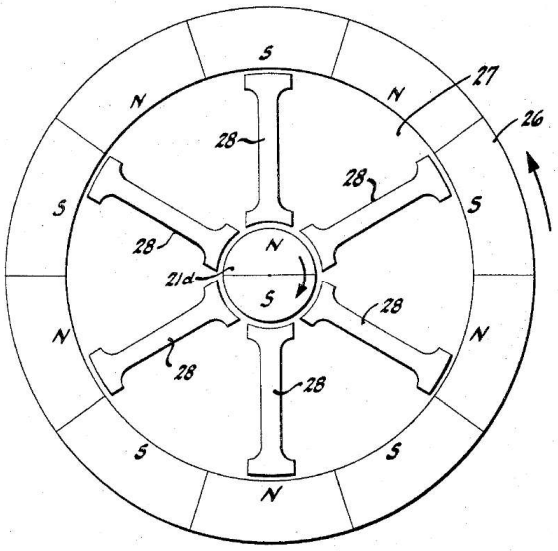

Figure 2.3: Close-up of the patent showing the first use of pole-pieces [43]

Concurrently, the development of magnetically gear integrated PDD machines started, with the first design being published in 1993 by Venturini, where a magnetic gear was integrated in an axial flux direct-drive machine [48]. The topologies changed into coaxial ones starting in the later half of 2000-2010, with the first patent being filed in 2004 [49]. It was Atallah however who introduced the outer stator PDD machine seen in Figure 2.4 in his 2008 paper [50], which would later be used in the INNWIND project, which will be discussed later in this chapter.

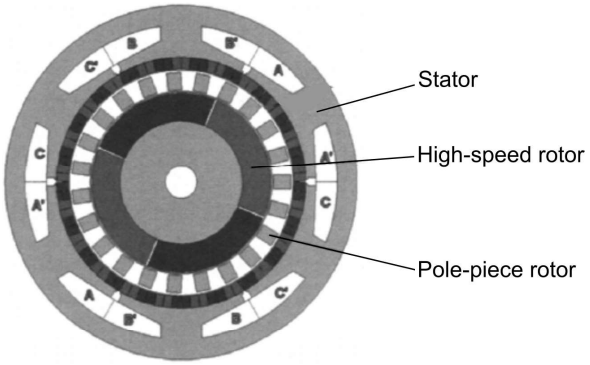

Figure 2.4: Pseudo direct-drive topology introduced by Atallah. Based on [46]

2.2 Working Principle

Since a PDD machine is a relatively novel design, first mentioned in 1993 [48], and because of its complex interaction of magnetic fields, it is not that straightforward to understand the working principle of a PDD machine. Therefore, the aim of this section is to provide a basic understanding of the working principles of the magnetic gear.

In 2001, Atallah was the first one to reveal the potential of the magnetic gear topology which is widely used now [46]. Because of this, the explanation of the working principle will be focused on his topology. The concentric magnetic gear has three parts, which can be seen in Figure 2.4: the high-speed rotor on the inside, the stator on the outside, and a low-speed or pole-piece rotor in between them. It should be noted that it is also possible for the pole-piece rotor to be static while the outside 'stator' can be the low-speed rotor. However, the former configuration is more common. In a PDD machine, the pole-piece rotor consists of a certain number of iron or steel blocks, of which the number is calculated by

$$q_{pp} = p_i + p_o \tag{2.1}$$

Where q_{pp} is the number of pole-pieces, p_i and p_o the number of pole-pairs on the inner and outer permanent magnet array, respectively. By keeping this ratio of pole-pieces and pole pairs, the pole-piece rotor modulates the magnetic field from one rotor to the other. The modulation will cause the magnetic field of one side to be modulated, so that the other side sees a space harmonic corresponding to its own number of poles.

When the outer ring is stationary, the gear ratio G between the inner high-speed rotor and the pole-piece rotor is

$$G = \frac{q_{pp}}{p_i} \tag{2.2}$$

Another, more logical way to look at the working principle is to imagine the pole-pieces are equivalent to the planet gears in a mechanical planetary gear, with the magnetic field in them rotating instead of an actual round array of magnets as seen in Figure 2.5. The inner permanent magnet array translates to the sun gear in the mechanical equivalent, while the outer permanent magnet array translates to the ring gear of the mechanical equivalent, as can be seen in Figure 2.6a and 2.6b. The rotating magnetic field in the pole-pieces is then responsible for the gearing up of the high-speed rotor.

Figure 2.5: Mechanical planetary gear and its direct magnetic equivalent [18]

Since the magnetic gear transfers the power without physical contact points, the separate parts of the machine can rotate independent from each other, from a preferred relative position where the magnetic forces are in balance and no torque is transferred, to a relative position

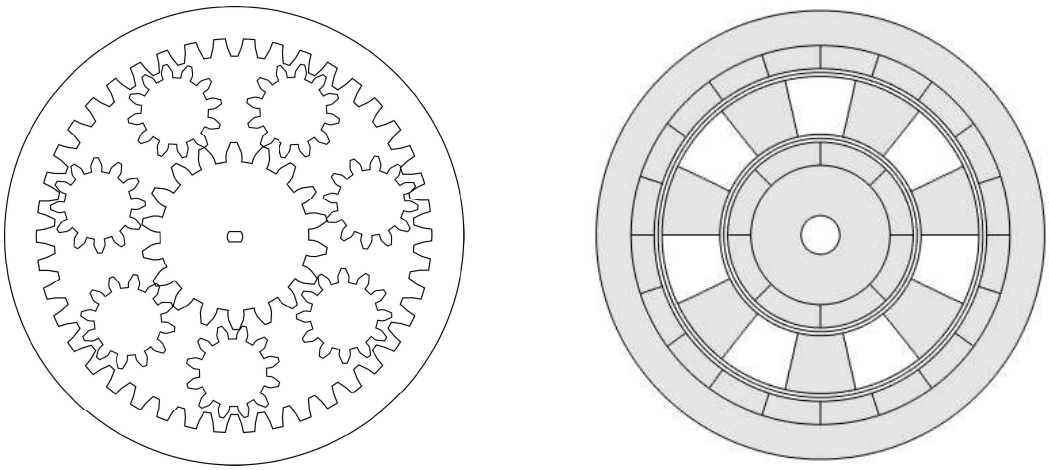

(a) Mechanical planetary gear

(b) Concentric magnetic gear

Figure 2.6: Mechanical magnetic gear and its improved magnetic equivalent

where the magnetic forces create a net torque, resulting in power being transmitted. This means that, just like a direct-drive machine, the magnetic gear has a sinusoidal torque-angle characteristic, as can be seen in Figure 2.7.

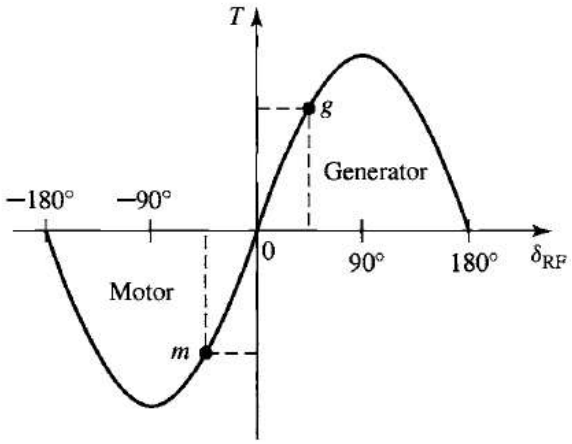

Figure 2.7: Sinusoidal torque angle characteristic of a synchronous machine [51]

Adding stator coils which magnetically link with the high-speed rotor now results in a PDD machine. Where the magnetic gear has a shaft connected to each of the rotors, the PDD machine only has one shaft exiting the machine, connected to the pole-piece rotor (in the case of the machine discussed in this report), while the high-speed shaft is only used to support the high-speed rotor internally. The high-speed rotor is thus rotating freely around its axis. In order for the high-speed rotor to be in equilibrium, the mechanical torque created by the magnetic gearing needs to be in balance with the electromagnetic torque created by the stator coils.

The advantage of the PDD machine is that because of the magnetic gear, the high-speed rotor rotates much faster compared to a direct-drive machine, which quickly becomes very

bulky when scaling up. By increasing the rotational speed, the required torque to deliver a certain amount of power decreases, which means the size of the machine decreases as well. This is how a PDD machine achieves its high torque density, and why it has become a very interesting topology for large wind turbines.

2.3 INNWIND Project

While the goals concerning the installation of wind energy were already set high, new figures show those efforts need to increase even further, as explained in Chapter 1. In order to meet those ambitious goals, it was quickly realised that there was not only a need for increased production, but also technological advancements, keeping in mind offshore projects can take up to 10 years from planning to commissioning [4]. In 2012, the INNWIND project was started, being a collaboration between 28 partners from both industry and academic institutions. The focus of the INNWIND project was *"high performance, innovative designs of beyond-state-of-the-art 10-20 MW offshore wind turbines and hardware demonstrators of some of their critical sub-components"* [11]. First of all, it investigated the benefits of up scaling of wind turbines on the LCOE, before identifying the innovations to investigate.

Next to that, promising innovations in several fields were identified, such as new blade materials, floating wind turbine concepts, and new types of generators. One of those new types of machines are PDD machines. It was identified that due to its infancy, no established design rules or analytical models were developed yet which would enabling optimization. This was made into a separate work package. This work package was done by Penzkofer, supervised by Atallah [31]. The work package included making analytical electromagnetic models for 10 to 20 MW wind turbines, including loss calculations. The conclusion of the work package was a successful analytical model which can be used to optimise PDD machines ranging from 10 MW to 20 MW without the need for expensive FEA models, although the optimised designs were verified with FEA. However, the model relies on rectangular pole-pieces, and there was no mention of the mechanical performance of the optimised designs. This posed a scientific gap which will be the scope of this report.

Chapter 3

Underlying Theory and Tools Used

In this chapter, an overview of the mathematical theory used will be given. This includes the mathematical equations used in the electromagnetic and mechanical model, as well as the way finite element analysis tools are used to perform simulations, covering the methodology as well as the simulation settings.

3.1 Governing Equations

Ever since computers got more powerful, numerical analysis has become increasingly popular. This way, the computer does most of the work, and the user's effort is reduced. Because of this, it is very easy to get lost in what the computer is actually doing, while it is actually beneficial to know what equations are being solved in order to understand the results more thoroughly. Therefore, the equations used in the models will be discussed here.

3.1.1 Electromagnetics

The physics used in the electromagnetic part of the model are focussed on Maxwell's equations. They are rewritten so they can be solved by a numerical tool. The differential form of Maxwell's equations for a field with no charges and a uniform field in the axial direction are as follows:

$$\nabla \cdot \vec{E} = \frac{\rho_e}{\epsilon} = 0 \tag{3.1}$$

$$\nabla \times \vec{E} = -\frac{\partial \vec{B}}{\partial t} \tag{3.2}$$

$$\nabla \cdot \vec{B} = 0 \tag{3.3}$$

$$\nabla \times \vec{B} = \mu \left(\vec{J} + \epsilon \frac{\partial \vec{E}}{\partial t} \right) = \mu \vec{J} \tag{3.4}$$

Where $\vec{E}$ and $\vec{B}$ are the electric field strength and the magnetic flux density, respectively, while ρ_e and $\vec{J}$ are the enclosed electric charge and current density, respectively. Finally, ϵ and μ are the permittivity and permeability of the material the equations are applied in. In order to reduce this set of equation to solve for the magnetic field numerically, the magnetic vector potential $\vec{A}$ is introduced, which is defined as the curl of the magnetic flux density $\vec{B}$:

$$\vec{B} = \nabla \times \vec{A} \tag{3.5}$$

Using Equation 3.5 in Equation 3.3 shows that defining the magnetic vector potential like this is allowed:

$$\nabla \cdot \vec{B} = \nabla \cdot (\nabla \times \vec{A}) = 0$$

Now, using Equation 3.5 in Equation 3.4 results in

$$\nabla \times \vec{B} = \nabla \times (\nabla \times \vec{A}) = \nabla(\nabla \cdot \vec{A}) - \nabla^2 \vec{A} = \mu \vec{J}$$

Applying the Coulomb gauge condition ($\nabla \cdot \vec{u} = 0$) simplifies the equation further:

$$\nabla(\nabla \cdot \vec{A}) - \nabla^2 \vec{A} = -\nabla^2 \vec{A} = \mu \vec{J} \tag{3.6}$$

which is the Laplacian of the magnetic vector potential $\vec{A}$. $\vec{J}$ is the source term for the model, which can consist of a physical current density and the magnetization $\vec{M}$ of the magnet. This means $\vec{J}$ becomes

$$\begin{aligned}
\vec{B} = \mu \vec{H} + \vec{B}_r = \frac{1}{\mu}\vec{B} &= \vec{H} + \vec{M} \\
\nabla \times \vec{H} = \nabla \times \left(\frac{1}{\mu}\vec{B} - \vec{M}\right) &= \vec{J}_e \\
\nabla \times \frac{1}{\mu}\vec{B} &= \vec{J}_e + \nabla \times \vec{M} \\
\nabla \times \vec{B} &= \mu\left(\vec{J}_e + \nabla \times \vec{M}\right) \\
\Rightarrow \vec{J} = \vec{J}_e + \nabla \times \vec{M} &= \vec{J}_e + \nabla \times \frac{1}{\mu}\vec{B}_r
\end{aligned} \tag{3.7}$$

Where $\vec{J}_e$ is the physically applied electrical current density in the coils, and $\vec{B}_r$ the remanent flux density of the permanent magnets. This means COMSOL will solve following equation:

$$-\nabla^2 \vec{A} = \mu \vec{J}_e + \nabla \times \vec{B}_r \tag{3.8}$$

When the system is solved, the magnetic flux density can be derived from the magnetic vector potential using Equation 3.5.

3.1.2 Mechanics

Whereas in the electromechanical model, an Eulerian formulation is used focusing on the flux through an element, a Lagrangian formulation is used for the mechanical model. The Lagrangian formulation focusses on the movement of each element rather than the flux through it [52]. This means Newton's second law can be applied directly. Although, because of discretization done in finite element analysis, it is more convenient to use a formulation per unit volume. Therefore, the equation used in COMSOL is:

$$\rho \frac{\partial^2 \vec{u}}{\partial t^2} = \nabla \cdot \vec{S} + \vec{F}_v \tag{3.9}$$

where ρ is the local density of the material, $\vec{u}$ the displacement vector, $\vec{S}$ the local stress tensor and $\vec{F}_v$ the applied body load [53]. It should be noted that the stress tensor $\vec{S}$ is also called the second Piola-Kirchhoff stress, which differs from the Cauchy stress. The latter one is the 'true stress' expressed in the spatial frame which relates to the initial state of the model, whereas the Piola-Kirchhoff stress is expressed in the material frame, which means it relates only to the local stresses and deflections in the material. This makes it easier to see the interactions between the elements, and takes care of non-linearities when large deflections occur [54].

Next to the equation used in COMSOL, for verification purposes, a couple of other equations are used as well. Since the mechanical model consists mostly of beams clamped at both ends, as will be discussed in Chapter 4, some analytical equations can be used to verify some results. One of the simplest ways to verify the mechanical model, is to simulate a case where the model is loaded with a static force, and verifying the deflection analytically, which is done with the following equation:

$$u = \frac{qL^4}{384EI} \tag{3.10}$$

Where u is the static deflection of the middle of the beam, q is the loading on that beam, L the length of the beam, E young's modulus of the beam material, and I the area moment of inertia of the beam cross-section. The latter two combined (EI) can be called the beam's stiffness [55, 56]. While this equation is very simple, it also relies on a lot of assumptions, such as:

- The beam material is isotropic, i.e. the material properties are the same in every direction
- The beam material is homogeneous, i.e. the material properties are constant throughout the whole body
- The beam cross-section is constant
- The applied load is uniformly distributed

Next to that, Equation 3.10 only gives the deflection in the middle of the beam, which, using the mentioned assumptions, is also the maximum deflection of the beam.

Since the scope of the report is focused on the dynamical deflection of the pole-pieces, simple yet useful values to calculate are the natural frequencies of the model. These natural frequencies are important for any mechanical design, because when a mechanical part gets excited at its natural frequency, resonance occurs, which can have disastrous effects [57]. This resonance can occur at different frequencies, at which point different so-called modes of resonance occur, as seen in Figure 3.1.

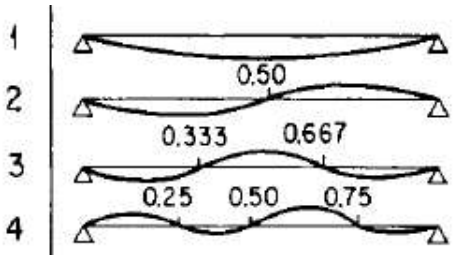

Figure 3.1: Example of modes of vibration [59]

In this case, the driving force is the electromagnetic force, which is evenly applied to the whole pole-piece. Since the force will always come from the same side, it can be seen that the odd modes in Figure 3.1 will be the more sensitive to excitation than the even modes, since they require a force coming from different sides, applied to different points along the length of the pole-piece.

For verification purposes, calculating the natural frequencies can be done analytically:

$$\omega_n = \beta_n^2 \sqrt{\frac{EI}{\rho L^4}} \tag{3.11}$$

Where ω_n is the natural frequency of the beam and β_n the vibration coefficient of the beam. This coefficient depends on the beam configuration, which in this case is assumed to be clamped at both ends. The coefficient is given in several books like [58], but can also be approximated by

$$\beta_n = \frac{(2n+1) \cdot \pi}{2} \tag{3.12}$$

where n is the mode number [59]. This way, any number of natural frequencies can be calculated analytically.

3.2 Finite Element Analysis

In this part, the methodology of finite element is discussed in order to give an overview of everything going on behind finite element analyses. Since COMSOL is a comprehensive tool that includes all possible settings, the most important ones are also discussed to make it easier to reproduce the results found in this report.

3.2.1 Methodology

When starting off with finite element analysis, any tool might seem very daunting. However, after getting familiar with the basics of finite element analysis, it can easily be broken down into parts. These parts are shown in Figure 3.2 where the relations between all the steps are illustrated as well. Each step and the way it is implemented in COMSOL will be explained here.

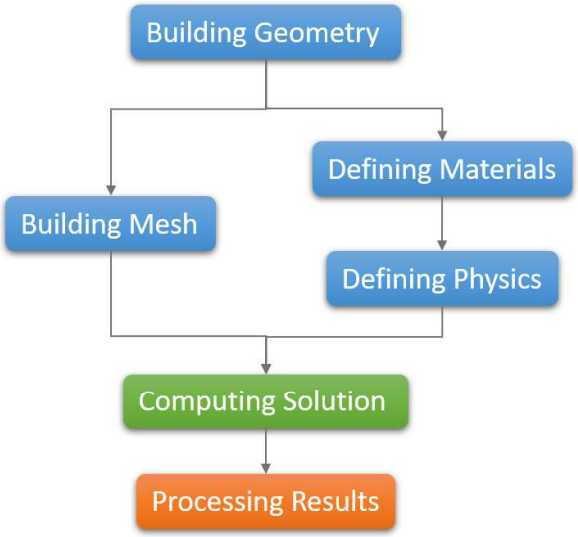

Figure 3.2: General workflow of a finite element analysis tool

First of all, a geometry of the model needs to be defined. This geometry is a graphical representation of the system to be analysed. This geometry can be built in different ways. In the case of the electromagnetic model considered in this report, a two-dimensional model was used, whereas for the mechanical model, a three-dimensional model was used. Both types of models start off the same way, by sketching the geometry of the subject to be analysed. In the case of the three-dimensional model, this sketch can then be extruded.

When the geometry is finalized, the materials used should be defined. In this case, all of the materials were built-in in COMSOL. Defining the material only means that the domains of the respective material should be selected, so it is known by the solver what properties to assign to each domain.

Next, the physics can be defined. The type of physics which should be implemented is dependent on the goal of the model and solution. In the case of the electromagnetic model, the *Rotating Machinery, Magnetic* physics was used, whereas for the mechanical model, the *Solid Mechanics* physics was used. Either of these have the minimum required physics nodes included, in order to make sure all domains are defined in the physics. Next to those nodes, other features have to be defined, such as the remanent flux density of the permanent magnets or a non-linear BH-curve in some of the domains of the electromagnetic model, or body forces in the mechanical model. Additionally, nodes have to be added in the electromagnetic model for force calculations. These nodes calculate electromagnetic forces which are then made accessible in the results.

The last step to build a model used in finite element analysis is building a mesh. Building a proper mesh is an art on its own, so only a brief explanation will be given here. The main principle of finite element analysis is to discretize the domains into smaller, finite domains, called elements. The field to be solved for, being a magnetic potential or displacement, will then be computed on the corners of these elements, called the nodes. The trade-off that occurs when discretizing is accuracy versus computational effort. Discretizing the model into very small elements will result in an accurate solution, but it will require a lot of computational resources to solve. On the other hand, having bigger elements and hence a model using less computational resources will result in less accurate results. In order to have an efficient as possible mesh, a user-controlled mesh was used in COMSOL, where different discretization was applied to different domains, in order to increase accuracy where needed, and increase the mesh quality where possible. It should be noted that building the mesh can already be done right after building the geometry, as no material or physics properties are required for building the mesh.

When all the step are taken to build the model, the solution can be computed. In this case, since the model is a rotating machine, solving the model consists of different so-called study steps. First of all, a *Stationary* study step is used to calculate the initial, stationary condition of the model before using it in a *Time Dependent* study step. The *Time Dependent* study step is needed to simulate the time-dependent rotation of the machine. This means the machine will be rotated in discrete angles, and for each angle, the fields to be solved for are calculated again. Each of these study steps have a multitude of setting, which will be discussed in the next section.

Finally, when the simulation is done and the solution is computed, results are available. In COMSOL, this does not mean anything is visible yet, as the data of interest needs to be extracted from the data sets. This can be done in the form of two-dimensional plots showing the magnetic flux density, current density, etc., one-dimensional graphs showing the magnetic field along a certain line or graphs showing the deflection of some point of the model over time.

Sometimes, each of these steps need to be done in different user interfaces or even tools depending on what finite element analysis tool is used. In COMSOL however, building, simulating and processing results from a model are all done in the same user interface. A *Model Builder* tree is used to get an overview of all the steps explained before, as can be seen in Figure 3.3.

The model builder tree seen in Figure 3.3 is a simple example and not the one used for the analyses performed in this report. All previously explained steps can be found in the tree, with the addition of some more nodes which are used for parametrizing and making handling the model more convenient.

3.2.2 Simulation Settings

Solving a model or running a simulation can be pretty straightforward with COMSOL, since it suggests a solver based on the physics being used. However, sometimes this results in slow and even poor convergence when COMSOL prioritizes robustness over speed and computational resources. Because of this, the solver was customised. Both the solver of the *Stationary* and *Time Dependent* time step use a direct solver.

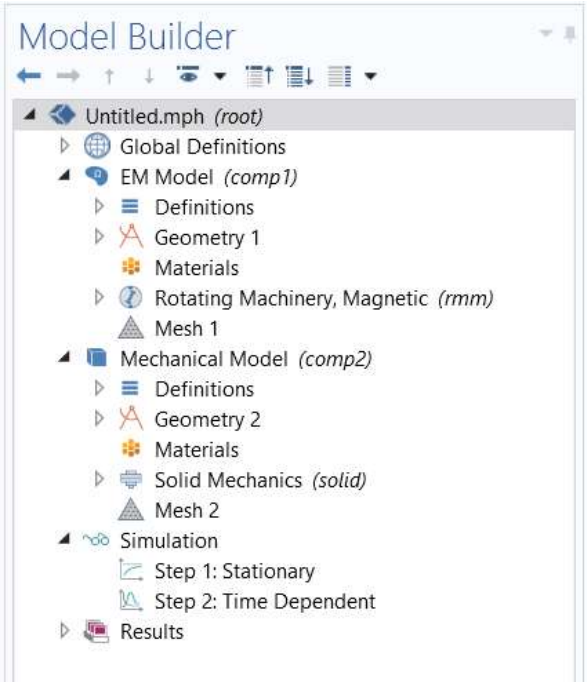

Figure 3.3: Example of the Model Builder tree in COMSOL

Direct solvers have the advantage of being faster than iterative solvers, but they do require a lot of internal memory (RAM) [60]. When the available RAM is insufficient for the model, the solver will offload part of the solution on the external memory (hard disk or SSD), which slows down the process a lot. However, for most of the models the available RAM was sufficient, so a direct solver was chosen. COMSOL offers several direct solvers, but PARDISO was chosen for its speed compared to the other options. Next to that, the option to store part of the solution on the external memory was turned off for the above mentioned reason.

Additionally, a fully coupled approach is preferred over a segregated approach. This could be somewhat surprising since the segregated approach can split multiple physics and solve them separately. However, it had been verified that the fully coupled method, where all physics and components are solved for at the same time, is at least twice as fast [61]. With these settings, it is made sure that the simulation is run efficiently.

3.2.3 Manipulation for Certain cases

While the modelling and simulating can be relatively straightforward, there are some cases that need special attention, where the parameters of interest cannot be obtained without further manipulation of the model or results. These cases are discussed here.

Arkkio's Method for Torque Calculations

In order to calculate the torque in a more accurate way than the method used by COMSOL, which is based on integration of the Maxwell tensor, Arkkio's method is used [62]. Using

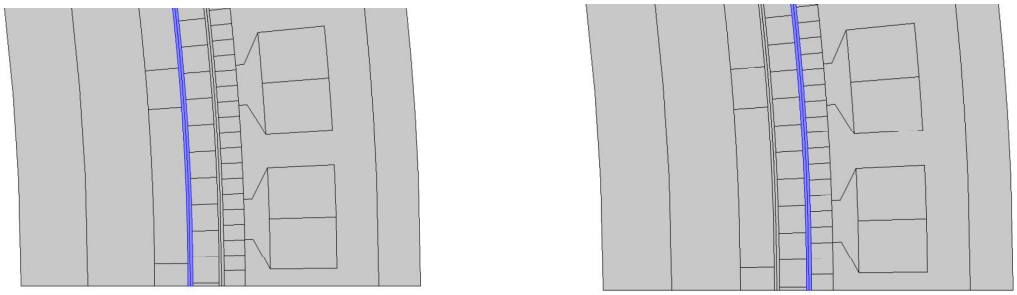

(a) Inner air gap surface

(b) Outer air gap surface

Figure 3.4: Surfaces used for Arkkio's torque calculation method

this instead of the build-in method allows a more stable result, because the Maxwell tensor method uses a line integral, while Arkkio's method uses a surface integral, as seen in Equation 3.13. This added integration will smooth out errors in the torque created by discretizing the magnetic field in a mesh.

$$T = \frac{l}{\mu_0(r_{out} - r_{in})} \int_S B_{rad} B_\theta r dS \tag{3.13}$$

Where l is the machine length, r_{out} and r_{in} the outer and inner air gap radii, respectively, B_{rad} and B_θ the magnetic flux density in the radial and tangential direction and S the air gap surface. Since a pseudo direct-drive has two air gaps, Arkkio's method is also applied to two surfaces. The surfaces used in the model are shown in Figure 3.4.

Now, from these surfaces, al the necessary torque quantities can be derived. The high-speed rotor torque is directly found by applying Arkkio's method to the inner air gap. The torque on the pole-piece rotor is found by applying Arkkio's method to the outer air gap and subtracting the high-speed rotor torque.

Figure 3.5: Different torque quantities described

Balancing High-speed Rotor Torque

In a pseudo direct-drive, the high-speed rotor is supposed to be freely rotating. This means that the magnetic torque exerted by the low-speed rotor by modulating the magnetic fields should be equal but opposite to the electromagnetic torque exerted by the magnetic fields generated by the stator coils. This means the high-speed rotor has two torque angles, one that adjusts the magnetic torque, and one adjusting the electromagnetic torque. At any given operating point, given that the magnetic torque is lower than the pull-out torque, the high-speed rotor will adjust its relative angle so that the magnetic and electromagnetic torque balance each other.

Because of the way the torque and current angle are implemented in combination with a simple time dependent analysis where the rotors and magnetic fields rotate at one specified speed, the net torque on the high-speed rotor will not always be zero. This can be due to small deviations and noise which are inherent of finite element analyses. Next to that, the current angle needed to be set manually, so it might be possible the electromagnetic torque is not perfectly tuned. Because of this, the high-speed rotor might have some residual torque. While this torque might seem insignificant being only a fraction of a percent of the nominal low-speed rotor torque, it should be kept in mind that the gearing ratio will amplify this residual torque, which can then affect the efficiency with a few percent. In order to cope with this issue, it is assumed that the small residual high-speed rotor torque can be multiplied with the gearing ratio, and then added to the low-speed rotor torque. This way, the torque balance on the high-speed rotor is taken into account for the efficiency and mechanical torque calculations. It should be kept in mind that one important assumption was made here: The small residual torque would need to have been cancelled by a very small shift in the mechanical torque angle, which would affect the magnetic field, and might impact the efficiency and torque calculations as well. However, since the shift is negligibly small, it is assumed the magnetic fields are not affected in a significant way. During the verification process, the measured torque will be used, while for quantifying the properties of the mechanical models, the calculated torque will be used.

Calculating the Electrical Parameters

In order to calculate the electrical parameters such as inductance and induced voltage, some steps needed to be taken before these parameters could be extracted. The induced voltage was calculated by setting the coil currents to zero, and measuring the voltage induced by the permanent magnets on the high-speed rotor. The inductances were calculated in a somewhat more complex way. In order to make sure the moving magnets of the high-speed rotor would not induce a voltage and affect the inductance, the permanent magnets were turned off by setting their remanent flux density to zero. Then, to calculate the self-inductance of the coils, the current through two phases of coils was set to zero, after which the inductance could be calculated by dividing the flux linked by the coil by the current through the coil. The mutual inductance was then calculated by measuring the flux through another coil, and dividing that by the current through the first coil.

Chapter 4

Pseudo Direct-drive Modelling

This chapter covers how the electromagnetic and mechanical models were built and set up. Next to that, the verification process of the models will be explained. For the electromagnetic model, this means both the operation as a magnetic gear, as well as the operation as a pseudo direct-drive will be covered. The chapter ends with a discussion of the simulation results of the design proposed by INNWIND.

4.1 Scope of the Model

There is no limit on how elaborate and accurate a physical device or phenomenon can be modelled. However, the modelling and following simulating will cost more resources the more elaborate the model becomes. Therefore, every model usually has its limits, which depends on the scope of the research and resources available. Also in the case of this research, there are limits.

One of those limits is that the electromagnetic model is only two-dimensional. The reason for this is that the available model in the INNWIND project is two-dimensional as well, which would make verification of a three-dimensional model difficult. Next to that, the computational resources needed for such a model were not available at the time of this research. It has been shown that a two-dimensional model overestimates the performance of a pseudo direct-drive machine by quite a margin, mostly due to edge effects. However, the behaviour is still the same, meaning that qualitative research can be done with a two-dimensional model [18]. Next to that, the biggest discrepancy between two- and three-dimensional models comes from edge effects from machines with a high aspect ratio, meaning flat machines with a relatively high diameter to stack length ratio. In the case of the INNWIND design, the radius is only about twice the stack length, meaning that the discrepancy between two- and three-dimensional analyses will most likely be less than described in literature.

As a result of the two-dimensional modelling, only a one-way coupled analysis can be done, where the deflection of the pole-pieces depends on the magnetic fields, instead of doing a two-way coupled analysis, where the magnetic fields also depend on the deflection of the

pole-pieces. This is because the deflection of the pole-pieces is three-dimensional, since the deflection in the middle will be higher than at the edges, where the pole-pieces are fixed. This means that the larger the deflection is, the less accurate the model becomes, since with large deflections, the magnetic fields would be affected, and the electromagnetic forces could increase due to negative stiffness [35]. This is an extra motivation to keep the deflection of the pole-pieces as small as possible, in order to ensure the validity of the results.

Next to that, whenever efficiency is mentioned in the remainder of the report, it refers to the accuracy of the electromagnetic model. Due to numerical errors, it is possible for the model to not be 100 % efficient, but this does not say anything about the physical efficiency. In order to do this, separate analytical losses have to be done in combination with the two-dimensional model, which is not the scope of this report.

4.2 Electromagnetic Model

Since the proposed design of the model was focusing on the electromagnetic properties, the electromagnetic model is well thought out. This means that it is more complex than the mechanical model, and requires more attention to model and verify. In this section, the setup of the model will be discussed, including the verification of the model.

4.2.1 Electromagnetic Model Setup and Geometry

As explained before, the INNWIND design described in their report consists of a two-dimensional model. Since the air gap is much smaller than the machine length, it is expected that, relatively speaking, there will not be a lot of flux leakage. Next to that, since the analysis is only one-way coupled, there is no need to extend the model to a three-dimensional one.

In order to build up the model, the parameters described in the INNWIND report are used as starting point for this project, which are summarized in Table 4-1. The last five parameters are not explicitly stated in the INNWIND report, but some are based on figures, and are thus just an approximation of the INNWIND model. The slot area is found with the help of the rated power and voltage, using a 98.5 % physical efficiency mentioned in the INNWIND report, while the radial teeth length is found by tuning it so that the inductance matches the one given in the INNWIND report.

The parameters in Table 4-1 result in the geometry seen in Figure 4.1. In this figure, the different domains with different material properties can be seen, where light grey corresponds to iron, orange to copper and dark grey to steel. The other colours refer to the different magnetisation directions of the permanent magnets. There are four magnetisation directions because a Halbach array is used on the stator side permanent magnet array, which enhances the magnetic field. For the magnetisation direction, a cylindrical coordinate system is used in order to allow radial and tangential magnetisation.

Table 4-1: Parameters used for the modelling of the electromagnetic model

Quantity	**Value**	**Unit**
Rated power	10	MW
Rated speed of pole-piece rotor	9.65	rpm
Rated torque on the pole-piece rotor	9.9	MNm
Analytical pullout torque	11.9	MNm
Rated electrical output frequency	48.25	Hz
Gear ratio	7.5	-
Pole-pairs on high-speed rotor per section	2	-
Pole-pairs on stator per section	13	-
Halbach segments per pole-pair on the stator	4	-
Pole-pieces per section	15	-
Number of identical sections	20	-
Pole-piece slot opening angle	$\pi/300$	rad
Airgap diameter	6.0	m
Radial thickness of pole-pieces	31.4	mm
Radial thickness of high-speed rotor PMs	39.8	mm
Radial thickness of stator PMs	25.2	mm
Length of inner air gap	6.0	mm
Length of outer air gap	6.0	mm
Active axial length	1.66	m
High-speed rotor pole arc to pole pitch ratio	0.8	-
Remanence of PMs	1.25	T
Relative recoil permeability of PMs	1.05	-
Copper packing factor	0.5	-
Current density at rated power	2.0	A_{RMS} mm^{-2}
Slot area	0.0071	m^2
Radial teeth length	0.08	m
Yoke thickness	0.1	m
Salient pole radial thickness	0.03	m
Stator pole arc to pole pitch ratio	0.6	-

4.2.2 Material Properties

Whereas for air, iron and copper, build-in COMSOL materials are used, the permanent magnet and steel materials are adapted from an existing material. The permanent magnet material was manually build based on air, since both have similar magnetic properties. The only parameter that changed, is the relative permeability, which was changed to 1.05 as given in Table 4-1. Next to that, the steel material was adapted as well. In order to model this material as accurately as possible, a non-linear material was used. However, since solid steel is mostly used for structural parts, the COMSOL default steel materials did not include a non-linear BH-curve. Instead, an HB-curve was added manually to the COMSOL material [63], which can be seen in Figure 4.2.

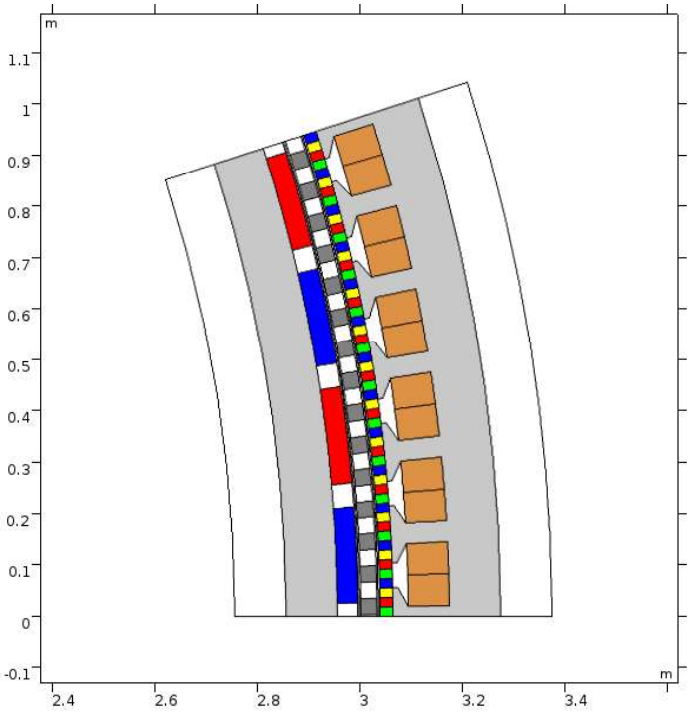

Figure 4.1: Geometry of one section of the machine investigated in this report

Since the exact steel alloy is not known, an average of the alloys in Figure 4.2 is used. While this means the material is still not modelled as accurate as it could be, it is much more accurate than using a linear material.

4.2.3 Meshing

In finite element analyses, meshing affects the computational effort to a great extent, as explained in Chapter 3. Too coarse, and the results will not be accurate enough. Too fine, and the computational effort will grow very fast. Finding a balance between these two extremes is an art in itself, but with some simple modifications, it is easy to reduce the computational effort greatly.

First of all, due to the large diameter of the machine compared to the model size, some of the domains are quasi rectilinear. This means their domain can be meshed with a rectangular mesh instead of a triangular one. This decreases the number of nodes necessary to mesh those domains. Next to that, the back iron of the high-speed rotor and the stator, where the magnetic field mostly changes in amplitude, but not direction, can be meshed much coarser than the air gap, where the magnetic field is changing very rapidly. Keeping these guidelines in mind, the mesh nodes seen in Figure 4.3 were created.

The first *Size* node sets the size of the following two nodes, which map one side of the mesh (the *Source*) to another side of the mesh (the *Destination*). This makes sure there is symmetry between the sides of the model to which symmetry can be applied. The following three nodes create a rectangular mesh on the pole-pieces and the space between them, the high-speed rotor magnets and the copper coils. Then, the air gap was meshed very finely in order to

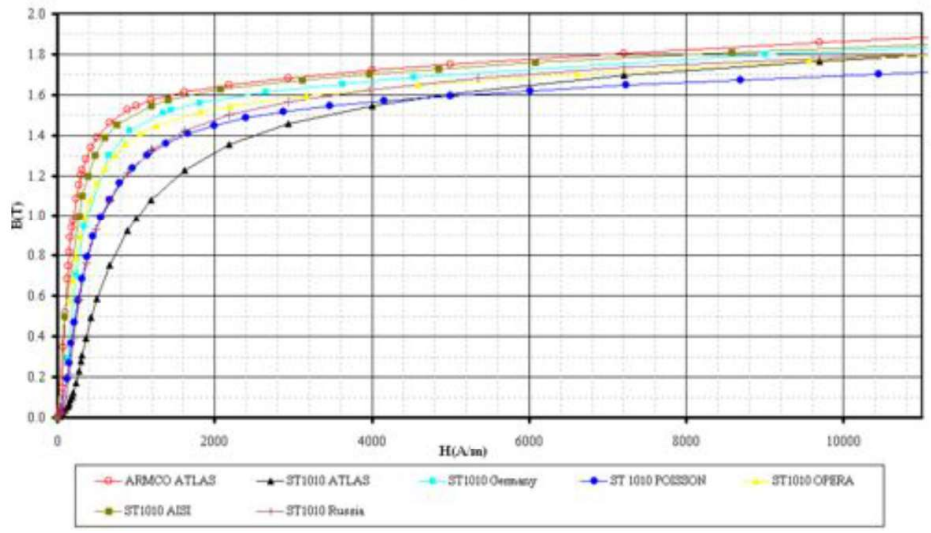

Figure 4.2: BH-curves of different steel alloys used as a reference (courtesy of A. Vorozhtsov) [63]

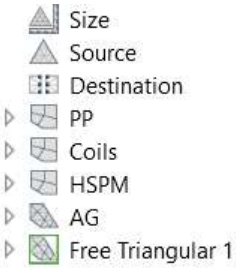

Figure 4.3: Model builder tree nodes used for the mesh of the electromagnetic model

ensure that the magnetic field in the air gap is calculated correctly, since this is an important area for every electromagnetic drive. Finally, the rest of the model is meshed with a very coarse mesh, since the sensitive areas are already meshed. Applying these nodes results in the mesh shown in Figure 4.4.

4.2.4 Setting the Rotor Angles for Nominal Operation

Since the model was built without keeping the relative position of the rotors in mind, the rotors might experience some torque even when no current is applied to the stator coils. This means that in order to ensure proper behaviour of the machine, the neutral position, or no-load position of the rotors had to be found. Since for a magnetic gear, the torque on the high-speed rotor is only dependent on the pole-piece rotor position, it is sufficient to only rotate the pole-piece rotor. This rotation was found manually, and when it was applied, the torque on the pole-piece and high-speed rotors were verified to be zero.

Next, as explained in Chapter 3, the torque and current angle has to be found for the machine to transmit torque. The electromagnetic torque angle is found keeping in mind that current is linearly proportional to torque [64, 65] for non-salient machines. Next to that, in the

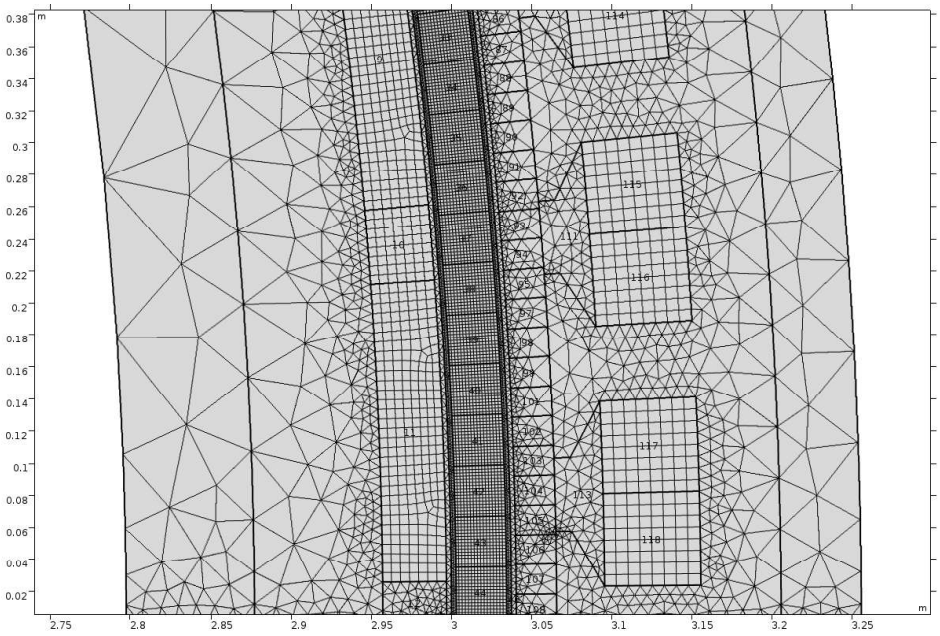

Figure 4.4: Close-up of the mesh for the electromagnetic model

INNWIND report, the pull-out torque is defined to be 11.9 MNm, whereas the nominal operating torque is 9.9 MNm at a current density of 2 A_{RMS} mm^{-2}. This means the current density to balance the high-speed rotor at the pull-out torque is 2.4 A_{RMS} mm^{-2}. From this, and keeping in mind the sinusoidal torque angle characteristic introduced in Chapter 2, the electromagnetic power angle can be calculated to be

$$\phi = sin^{-1}\left(\frac{J_{nom}}{J_{max}}\right) = sin^{-1}\left(\frac{2}{2.4}\right) = 0.985 \text{ rad} \tag{4.1}$$

Where ϕ refers to the rotation of the high-speed rotor and is expressed in radians, ranging from $-\pi$ to π. J_{nom} is the current density at the nominal operating point, while J_{max} is the current density at the pull-out torque of the magnetic gear. Since there are 20 identical sections with each of them having two sets of coils creating two electrical periods, and since the gearing ratio is causing the pole-piece rotor to rotate 7.5 times slower than the high-speed rotor, the mechanical torque angle is found to be

$$\alpha_{PP} = \frac{\phi}{2 \cdot s \cdot G} = \frac{0.985}{2 \cdot 20 \cdot 7.5} = 0.00328 \text{ rad} \tag{4.2}$$

Where α_{PP} represents the mechanical rotation of the pole-piece rotor from the neutral position in order to transfer the desired torque, while s is the number of symmetric sections in the model. It is chosen to only have this mechanical power angle for the rotors, and to adjust the electrical phase and thus electromagnetic torque to balance the high-speed rotor torque as explained in Chapter 3.

In applications like this, efficiency is important, and in order to reduce ohmic losses, *maximum torque per ampere* -control will be applied, which corresponds to having all the current in the

q-axis, and zero current in the d-axis, hence, this control scheme is sometimes called *zero d-axis current* control, or ZDC. In order to ensure this control scheme is applied, the current should be in phase with the induced voltage, which is the definition of the q-axis. Since the geometry of the model was build without keeping this in mind, the phase of the current was set manually. This was done by first checking the phase of the open-circuit induced voltage, by turning off the currents and measuring the induced voltage. Then, the current waveforms were given a manual phase shift so that it would be in phase with the induced voltage.

4.2.5 Electromagnetic Model Verification

When modelling anything, it should be verified whether the model behaves as it should. If the simulated result resemble values calculated analytically or experimentally (or obtained otherwise), it can be concluded that the model is indeed verified. In this case, the model is verified using the data given in the INNWIND report.

Magnetic Gear Verification

In order to verify whether the magnetic gear is properly modelled, the magnetic field is verified as much as possible. In the INNWIND report, graphs are given showing the radial magnetic flux density in the inner and outer gap. In Figure 4.5a and 4.6a, the radial magnetic flux density in the inner and outer air gap of the magnetic gear can be seen. The air gap magnetic flux densities seem to match the INNWIND graphs qualitatively, which can be seen in Figure 4.5b and 4.6b. Although, the match is not perfect, which can be explained by the fact that the mesh or integration method used in this research might differ from the one used in the INNWIND project. Next to that, the data was smoothed in order to get rid of noise generated by the fine mesh in the air gap, which filters out some details as well.

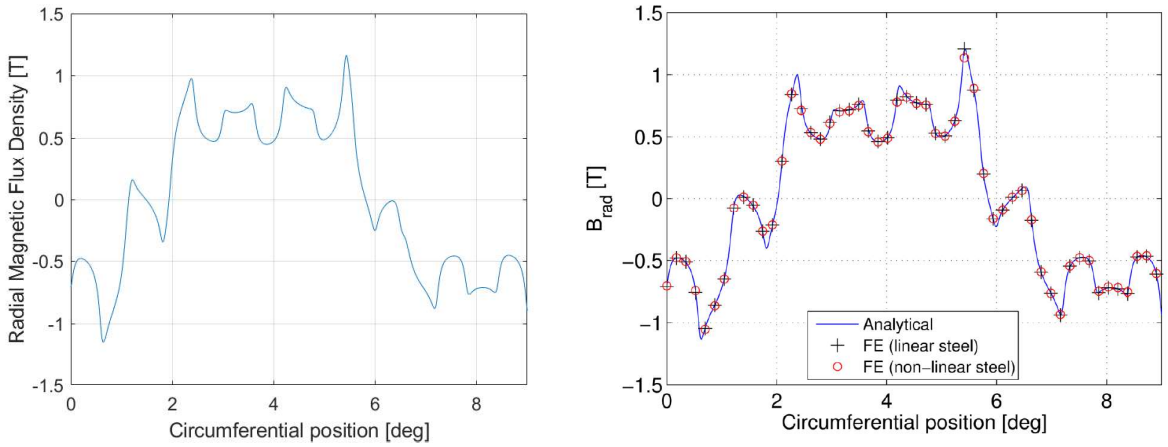

(a) Inner air gap magnetic flux density

(b) Inner air gap magnetic flux density according to INNWIND

Figure 4.5: Comparison of the inner air gap magnetic flux density of the model and the INNWIND project

Next to that, in the INNWIND report, two graphs are also given showing the torque ripple on the rotors. The low-speed rotor torque and high-speed rotor torque ripple is shown in

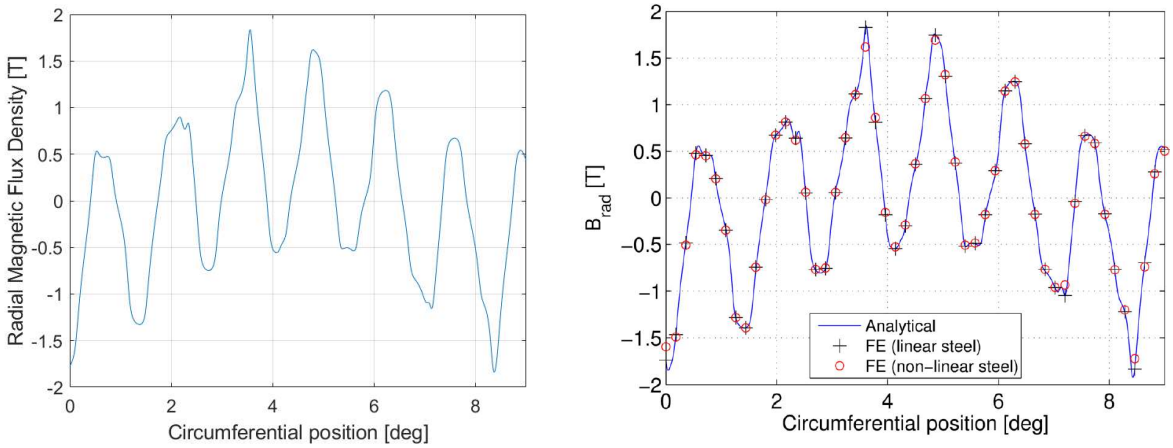

(a) Outer air gap magnetic flux density

(b) Outer air gap magnetic flux density according to INNWIND

Figure 4.6: Comparison of the Outer air gap magnetic flux density of the model and the INNWIND project

Figure 4.7a and 4.8a, showing one fifth of a magnetic period. Again, there seems to be a qualitatively good resemblance between the INNWIND design and the COMSOL model as can be seen in Figure 4.7 and 4.8. Especially the number of ripples and the magnitude of the ripples seem to correspond well. The shape is quite different however, which is mostly due to the meshing. When the meshing was refined, the waveforms started to resemble the waveforms given in the INNWIND report, but in order to save computational resources, the meshing was not refined any further. The torque can be seen to have a different amplitude, which can be explained by different BH-curves being used for the steel in this report. Since no exact type of steel is specified in the INNWIND report, this cannot be corrected.

Finally, the torque angle characteristic is checked. Since the load is transferred by magnetic forces like in a direct-drive machine, the torque angle characteristic can be expected to resemble a direct-drive torque angle characteristic. Looking at Figure 4.9, this is indeed the case, with a peak torque of 12.2 MNm on the pole-piece rotor. This is 2.5 % higher than the maximum value given in the INNWIND report, which is considered to be a small enough difference. On top of that, the torque is zero when no torque angle is present or when the torque angle is an integer multiple of π, which is the same behaviour found in direct-drive machines.

Pseudo Direct-drive Verification

After the operation of the magnetic gear is verified, the operation of the machine as a pseudo direct-drive can be verified as well. First of all, stator coils are activated. According to the INNWIND report, there are two coils per identical machine section, as seen in Figure 4.10, where each of the three phases are highlighted in a different colour. Each of these phases is fed with a sinusoidal current with an electrical angle of 120° from one another.

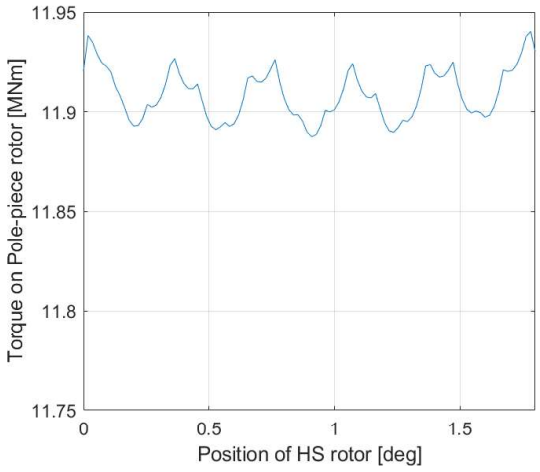

(a) Pole-piece rotor torque

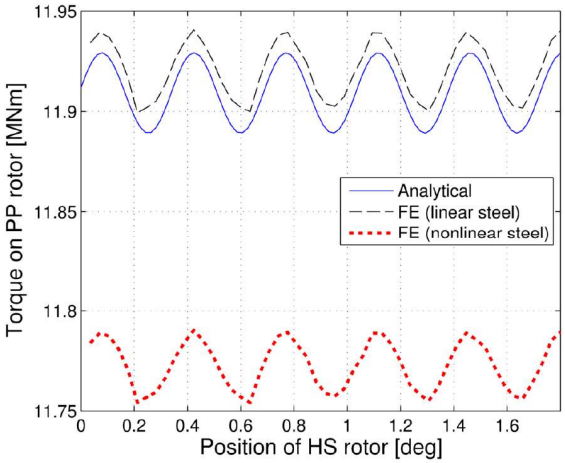

(b) Pole-piece rotor torque according to INNWIND

Figure 4.7: Comparison of the pole-piece rotor torque of the model and the INNWIND project

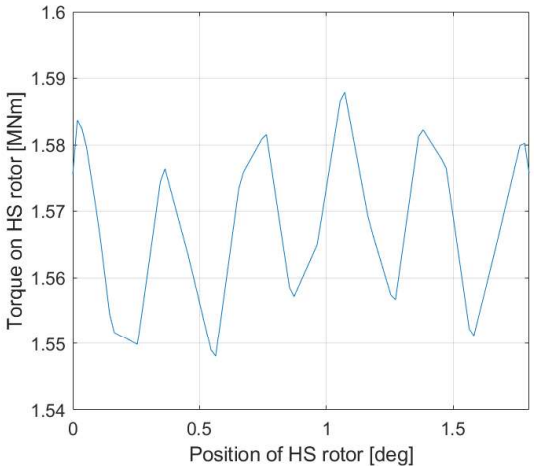

(a) High-speed rotor torque

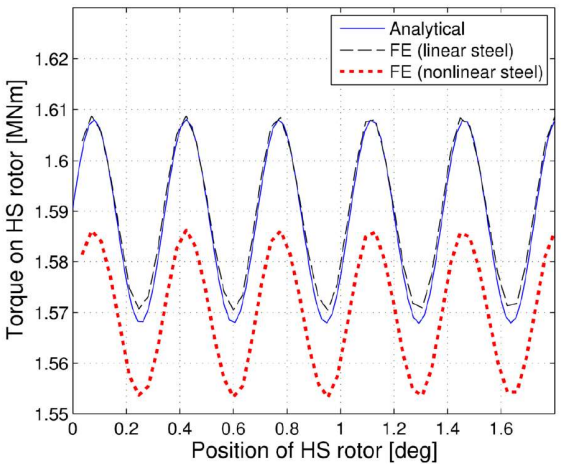

(b) High-speed rotor torque according to INNWIND

Figure 4.8: Comparison of the high-speed rotor torque of the model and the INNWIND project

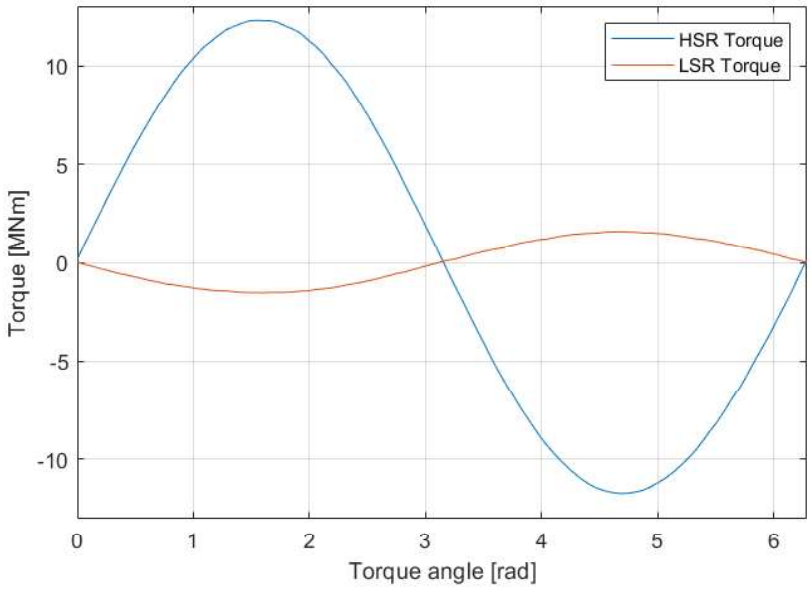

Figure 4.9: Torque angle characteristic of the magnetic gear

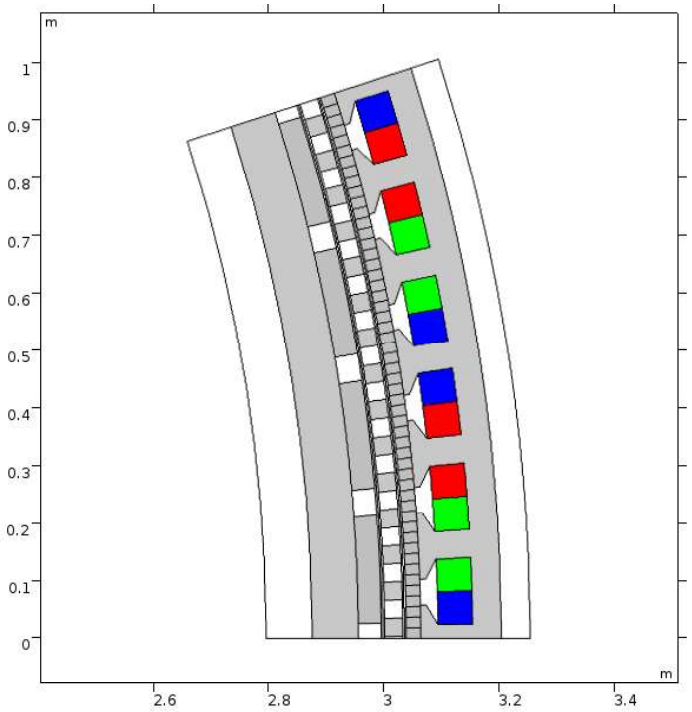

Figure 4.10: Cross-section of the geometry with the different phases highlighted in different colours

Electrical Parameters In the INNWIND report, a table is given with the electrical parameters of the machine, including inductances, resistance and induced voltage. From these, the self inductance was used to get the radial teeth length given in Table 4-1 by varying it and matching the resulting self inductance to the one given in the INNWIND report.

Table 4-2: Electrical parameters used for verification

Parameter	INNWIND value	Simulated value	Unit
EMF/turn/coil	24.0	23.3	V_{RMS}
Resistance/turn/coil	24.6	31.4	$\mu\Omega$
Self inductance/turn/coil	7.55	8.20	μH
Mutual inductance/turn/coil	-3.56	-3.57	μH

It can be seen that most of the values are relatively close to the values given in the INNWIND report, with the resistance being the only exception. Reasons for this might be a differently defined coil cross-sectional area or a non-standard copper conductivity value. Neither of these are explicitly mentioned in the INNWIND report, and since the resistance is much smaller than the reactance, it is chosen to leave the value as it is.

Power and Torque Balance The working principle of the pseudo direct-drive relies on the fact that the net torque on the high-speed rotor is zero, meaning that the magnetic torque exerted by the pole-piece rotor is cancelled by the electromagnetic torque produced by the stator coils. This means that for every operating point, a certain mechanical angle needs to be given to the pole-piece rotor in order to keep the balance. In order to get that angle, the torque angle relationship is used:

$$T = T_{max} sin(\phi) \tag{4.3}$$

Where T_{max} is the maximum torque exerted on the high-speed rotor. Next to that, as mentioned in the previous section, the electrical torque is linearly proportional to the current, and by extend, the current density [64, 65]. Using this in Equation 4.3 results in

$$\frac{J}{J_{max}} = sin(\phi) \tag{4.4}$$

Now, the torque angle ϕ refers to the rotation of the high-speed rotor and is expressed in radians, ranging from $-\pi$ to π. Using Equation 4.2, this can be translated back to mechanical degrees of the pole-piece rotor, which then results in

$$\frac{J}{J_{max}} = sin(\alpha_{PP} \cdot 2 \cdot s \cdot G) \tag{4.5}$$

$$\Rightarrow \alpha_{PP} = \frac{1}{2 \cdot s \cdot G} sin^{-1}\left(\frac{J}{J_{max}}\right) \tag{4.6}$$

Having the current loading as a parameter and rotating the pole-piece rotor according to this current loading allows the model to be run in any operating mode. Finally, in order to

check the proper operation of the pseudo direct-drive, the power balance is made to verify the efficiency. In order to do this, a time dependent simulation was run, since the position of the rotors relative to the mesh affects the efficiency by a few percent. In order to get rid of this effect, the average was taken of each time step over a couple of periods. Using the calculated torque explained in Chapter 3, the efficiency of the model turns out to be 99.2 %. It is very important to realise that this efficiency does not refer to the physical efficiency of the machine, but only the numerical accuracy of the model, as explained in Section 4.1. It should also be kept in mind that the meshing affects this value in the order of one or two percent. In order not to let this affect the results later in the report, the mesh is set as discussed before and kept the same throughout the rest of the report.

4.3 Mechanical Model

Since the report focuses on the dynamical mechanical behaviour of the pole-piece rotor, a correct mechanical model has to be made in order to produce relevant results. However, keeping the model as simple as possible is also important in order to reduce the computational effort and to focus on the important aspects. In this section, the build-up of the mechanical model will be discussed, as well as the verification process.

4.3.1 Mechanical Model Setup and Geometry

It was chosen not to include the flanges of the pole-piece rotor, since nothing is known about them, and optimising it would be to focus on mechanical engineering, which is out of the scope of this report. Thus, the focus is on the pole-pieces only, assuming the pole-piece attachment points are stiff. Additionally, since the mechanical deflection is not uniform along the length, the model cannot be simplified to a two-dimensional model like the electromagnetic model. Thus, the pole-pieces are modelled as an array of fifteen three-dimensional beams, as can be seen in Figure 4.11. The cross-section is based on the parameters given in Table 4-1, which results in a square cross-section with 31.4 mm sides.

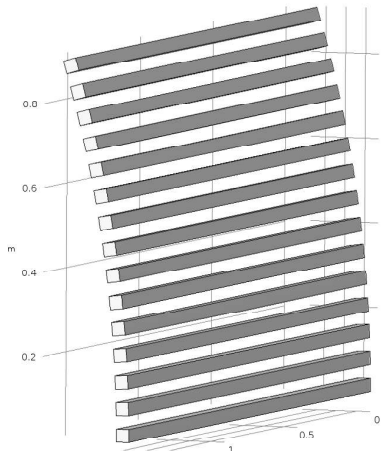

Figure 4.11: Geometry of the mechanical model used in this report

In the INNWIND design, the pole-pieces are decoupled, so for verification purposes, it would suffice to only model one pole-piece and check its behaviour over at least one magnetic period, given that its behaviour has already reached its steady state during that period. However, in order to improve the mechanical properties, which is a topic for Chapter 5, the pole-pieces are connected, and thus, all fifteen pole-pieces need to be modelled, since the same sector symmetry used in the electromagnetic model needs to be applied.

The physics applied to the mechanical model are equally simple. Both ends are assumed to be fixed in space. Whether or not this assumption is valid depends on the design of the pole-piece rotor flanges. If these are designed properly, the ends of the pole-pieces will move very little. However, if they are not properly designed, it is possible that the ends are allowed to rotate, which will allow much more deflection of the pole-pieces. However, since including the structural integrity of the fixtures of the pole-pieces would move the scope of the report to the field of mechanical engineering, it is left for future research. Next to the way the pole-pieces are fixed, the electromagnetic force on the pole-pieces is assumed to be homogeneous, since the electromagnetic force would only change at the ends of the pole-pieces due to electromagnetic edge effects. However, the ends of the pole-pieces are fixed anyway, which means the exact force at those ends is not as important as the forces in the middle of the pole-pieces. Hence, the electromagnetic force can be modelled as a homogeneous body load.

4.3.2 Material Properties and Meshing

Due to the simplicity of the model, only one material is used as described in the INNWIND model, which is steel. For mechanical analyses, the material can be considered isotropic and homogeneous.

Because of the nature of solid mechanics, the mesh of the mechanical model can be very coarse, because the deflection of beams is very gradual, without any sharp bends or corners. Because of this, a *Normal*-sized physics controlled mesh was applied in COMSOL.

4.3.3 Mechanical Model Verification

In order to verify whether the mechanical model works, some basic properties were verified. First of all, the static deflection was verified. This was done by applying a constant load to the beam, which is set to be 10 kN, since this is the order of magnitude of the applied electromagnetic force, as will be discussed in the next section.

The deflection can be calculated analytically by using Equation 3.10. In order to be able to calculate it, the area moment of inertia needs to be calculated:

$$I = \frac{a^4}{12} = \frac{0.0314^4}{12} = 8.10 \cdot 10^{-8} \text{ m}^4 \tag{4.7}$$

Where a is the length of one side of a pole-piece [56]. It should be noted that the area moment of inertia calculated here assumes the load is applied perpendicular on one of the sides of the pole-pieces, making the bending axis parallel with two of the sides. Using 205 GPa as the young's modulus for steel as given by COMSOL, the stiffness EI of the beam is found to be

16605 Nm^2. Then, the maximum deflection can be calculated to be

$$u = \frac{qL^4}{384EI} = \frac{F}{L}\frac{L^4}{384EI} = \frac{FL^3}{384EI} = \frac{10^4 \cdot 1.65^3}{384 \cdot 16605} = 0.00705 \text{ m}$$

The next step is to perform a stationary study with a body force of 10 kN on one pole-piece in the radial direction, making sure the load is applied perpendicular to one side. This results in a deflection of about 7.01 mm in the middle of the pole-piece. This is within one percent of the analytically calculated value, which means the static behaviour of the model is verified.

Also one of the main dynamic property of beams can be calculated analytically: their natural frequencies. Using Equations 3.11 and 3.12, this can be done analytically. Fist of all, the vibration coefficients of the beam need to be calculated. Since the electromagnetic load is assumed to be homogeneous, it is expected that only the odd modes will affect the dynamic behaviour of the beam. Hence, the first five resonance frequencies or modes will be calculated, in order to include the first three significant ones (first, third and fifth). Using Equation 3.12, the vibration coefficients are found to be

Table 4-3: The vibration coefficients of the first five natural frequencies

Mode	$\beta_n[-]$
1	22.2
2	61.7
3	121
4	200
5	299

Using these values, the beam stiffness calculated before and the density of steel ρ given by COMSOL, the five first natural frequencies of the beam are calculated. In COMSOL, the natural frequencies can be calculated in different ways. The most straightforward way is to do a separate *Eigenvalue* study of one pole-piece. The resulting natural frequencies, calculated analytically and simulated in COMSOL are shown in Table 4-4.

It can be seen that all frequencies are within 2 % of the analytically calculated values, with decreasing error for higher frequencies. This error is acceptable for finite element analyses, and the error for higher frequencies indicates good accuracy of the dynamical properties of the mechanical model. Another way to verify the natural frequencies is to check the frequency response of the pole-pieces. If the electromagnetic force has frequency components close to

Table 4-4: The first five natural frequencies, calculated analytically and simulated

Mode	f_n[**Hz**] **(calculated)**	f_n[**Hz**] **(simulated)**
1	59.4	60.5
2	165	167
3	323	326
4	535	538
5	799	803

the natural frequencies, resonance will be observed, which can also verify the analytically calculated frequencies. This will be done in the next section, where the results of the INNWIND design will be discussed.

4.4 Original Design Results

With the models build, simulated and verified, the results of the INNWIND design can be discussed. Since the results of the electromagnetic performance is already described in great detail in the INNWIND report, this part will focus on the electromagnetic forces acting on and deflection of the pole-pieces. In this and the following parts, the force and deflection will be decomposed in radial and tangential directions, since the focus is on the radial deflection as explained in Section 4.1. This decomposition is only done when post-processing the results after the simulation, since the deflection in both directions are not physically decoupled.

4.4.1 Pole-piece Force

Due to interaction of the pole-pieces with the electromagnetic fields, forces are induced. In contrast to ordinary permanent magnet machines, the pseudo direct-drive machine has two arrays of magnets. While this greatly increases the torque density of the machine, it also increases the magnetic flux density in the air gap, which results in higher forces, since the electromagnetic energy in the air gap is related to the magnetic flux density by

$$W_{EM} = \frac{B^2}{2\mu_0} \tag{4.8}$$

Where W_{EM} is the electromagnetic energy density in the air gap. Since the electromagnetic force is the same on every pole-piece, only shifted in time, the forces on only one of the pole-pieces will be discussed. These forces can be seen in Figure 4.12, where the electromagnetic force in the radial and tangential direction is shown.

In Figure 4.12, it can be seen that the forces in the radial and tangential direction reach values of about 18 kN and 19 kN, respectively. With these forces, a deflection of about 13 mm is expected in each direction separately, based on Equation 3.10. This is already much larger than the air gap of 6 mm allows. Looking at the total force on the pole-piece in Figure 4.13 however, it can be seen peaks of about 24 kN are reached. While this is a much higher force, not a lot can be said about how this influences the deflection, since the direction of the force is not known.

It is also useful to have a look at the frequency spectrum of the force, since it can already give a sense of whether resonance will occur, and can help verifying the deflection of the pole-pieces further. In Figure 4.14, it can be seen that the electromagnetic force has a strong 83 Hz component, with higher harmonics of this component present, as well as a less strong 19 Hz component. Both of these can be noticed in Figure 4.12.

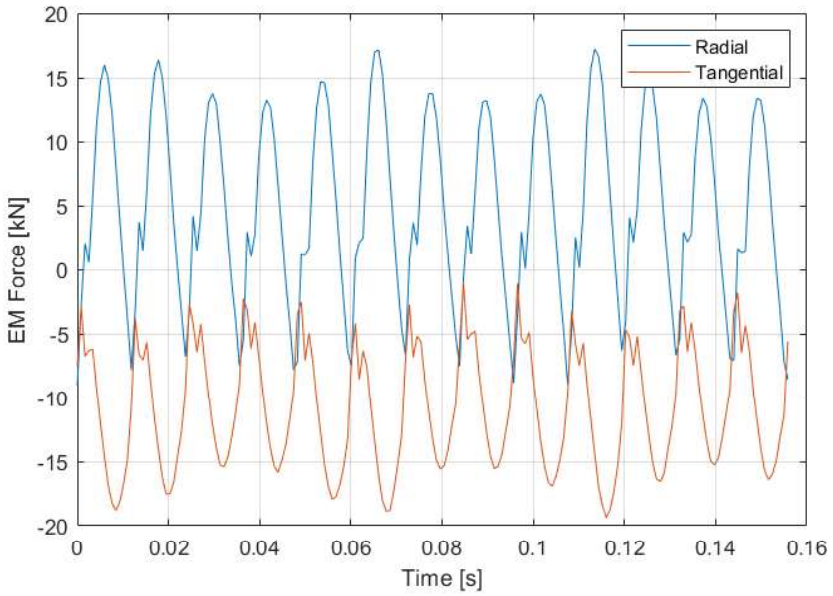

Figure 4.12: Time domain graph of the radial and tangential electromagnetic force on the pole-piece

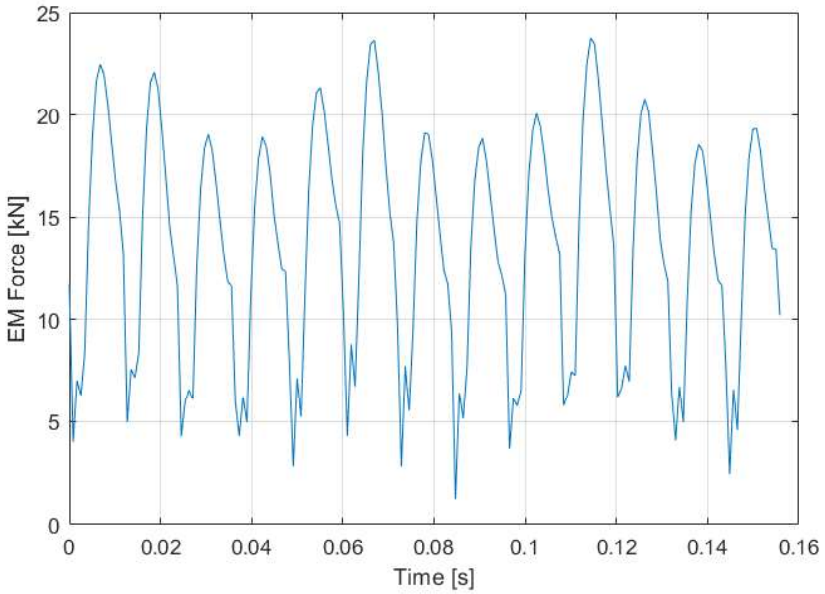

Figure 4.13: Time domain graph of the total electromagnetic force on the pole-piece

4.4.2 Pole-piece Deflection

In permanent magnet machines, the stators and rotors are mechanically very stiff, in contrast to the long, narrow beams that make up the pole-pieces. This makes mechanical analysis of the pole-pieces an important aspect when designing pseudo direct-drive machines.

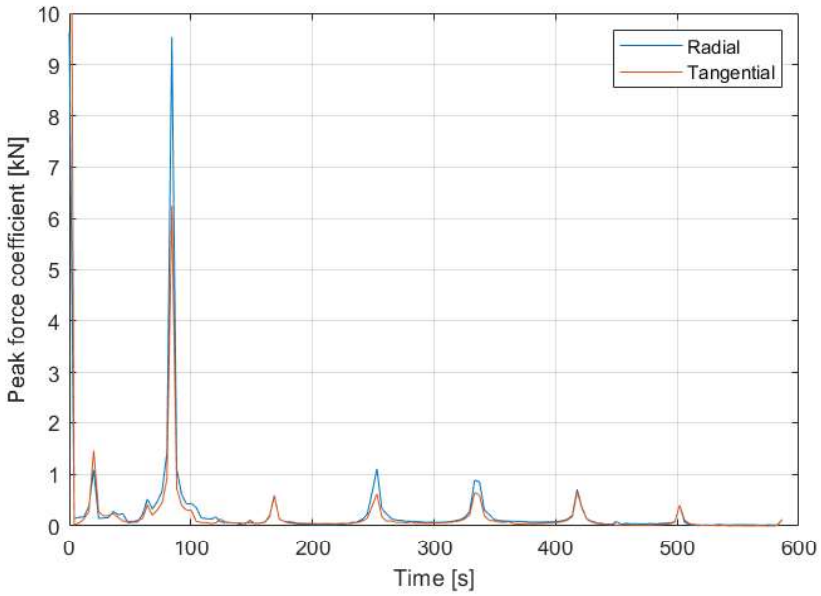

Figure 4.14: Frequency domain graph of the electromagnetic force on the pole-piece

Because of the type of analysis used, explained in Chapter 3, the deflection of the pole-pieces goes through a transient phase, before reaching steady-state. Since the transient phase of the analysis does not correspond to a real-life start-up situation, this part is not useful for quantitative mechanical analysis. Therefore, it is checked whether the deflection waveform has, in fact, reached steady-state, by comparing recurring periods of the deflection waveform.

Every of the fifteen pole-pieces experience the same previously described force, only shifted in time relative to the other pole-pieces. Next to that, because of this shift, each pole-piece starts off with a different steady-state deflection. These variables result in the deflection of each pole-piece being somewhat different, reaching slightly different values. The way to cope with this is to use a straightforward worst-case approach, where the pole-piece reaching the maximum deflection is used for further analysis. This means that while there are fifteen pole-pieces, and thus fifteen deflection waveforms, only one will be discussed in detail, while the others were only verified to check whether their results were reasonable.

The largest radial deflection reached in the INNWIND design is 31.2 mm, as can be seen in Figure 4.15, showing one steady-state period. This is a significantly higher deflection than the static deflection of 13 mm discussed before, and more than five times the airgap length. In the frequency domain, shown in Figure 4.16, the frequency spectrum of the deflection is shown. It can be seen that there are three distinct peaks at 19 Hz, 60 Hz and 83 Hz. These peaks are expected, as the peaks at 19 and 83 Hz correspond to the main frequency components of the electromagnetic force seen in Figure 4.14. The peak at 60 Hz corresponds to the first natural frequency of the pole-piece, which was calculated before to be 60.5 Hz. This confirms the verification done in the previous section. It is also verified that the frequency spectrum of the deflection of the other pole-pieces have a similar frequency spectrum, meaning that their behaviour is indeed similar to the one described here.

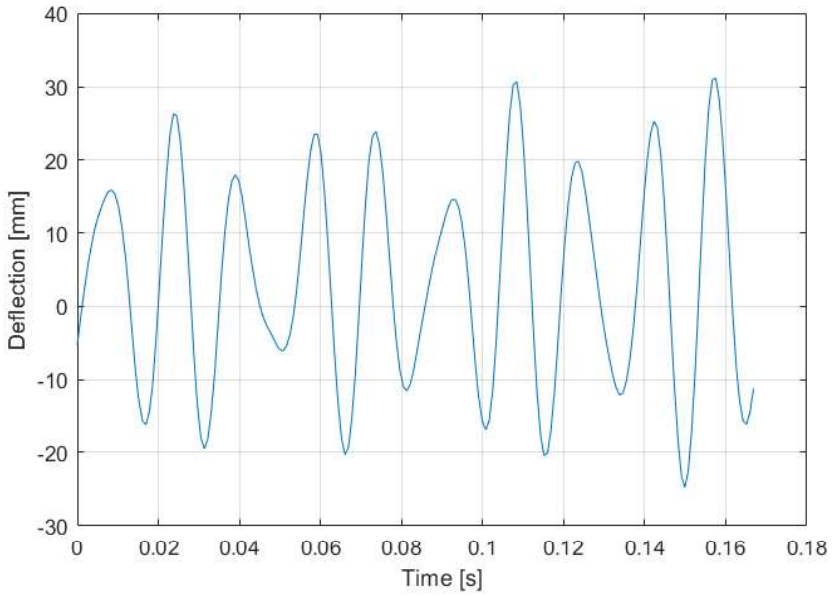

Figure 4.15: Radial deflection of the worst-case pole-piece

Another way to verify the mechanical model is to check the deflection coefficient for certain force coefficients. This can easily be done at 19 and 83 Hz. From Figure 4.14, it can be seen that the force coefficients reach values of 1.5 and about 7 kN, respectively. This corresponds, according to Equation 3.10, to a deflection of about 1 and 5 mm, respectively. These are indeed the values that can be observed in Figure 4.16, keeping in mind that at 83 Hz resonance starts playing a role, causing the peak at 83 Hz to sweep up a bit higher. This concludes that the original INNWIND design has big mechanical flaws, and cannot be implemented in a physical machine. In order to do so, the deflection needs to be reduced to only a few millimetres. Some approaches for this will be discussed in the next chapter.

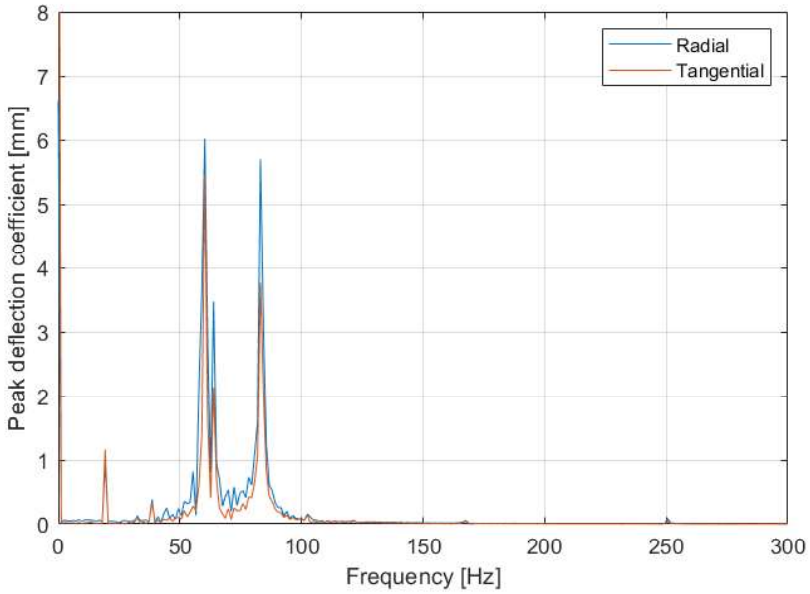

Figure 4.16: Frequency spectrum of the radial and tangential deflection of the pole-piece

Chapter 5

Improved Mechanical Models

As shown in Chapter 4, the deflection of the pole-pieces is greater than 30 mm, which is more than five times the air gap length. In order to make the INNWIND model physically feasible, a way to limit the deflection needs to be implemented. In this chapter, several ways of doing so are described first, after which their impact on the design is discussed.

5.1 Introduction of Improved Models

In order to understand the idea behind the suggested improvements, each model will be discussed here. The working principle behind every model will be explained, and the expected impact on the mechanical as well as electromagnetic performance will be discussed.

5.1.1 Elongated Pole-pieces

The first model focusses on increasing the stiffness by increasing the area moment of inertia. In the previous chapter, the area moment of inertia of a beam with square cross-section was given by

$$I = \frac{a^4}{12} \tag{4.7}$$

With a being the length of one of the sides. Now, when the cross-section changes to a rectangle, Equation 4.7 changes to

$$I = \frac{a^3 b}{12} \tag{5.1}$$

Where a is the length of the side along which the beam is bent, and b the length of the other side. This is illustrated in Figure 5.1 if the beam would be bent around the x-axis. If the beam would be bent around the y-axis, Equation 5.1 would become

$$I = \frac{ab^3}{12} \tag{5.2}$$

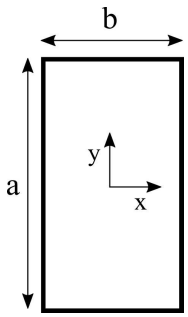

Figure 5.1: Beam with labelled axes and sides to clarify the concept of area moment of inertia

As can be seen, bending a beam along the longer side increases the moment of inertia compared to bending it along the shorter side, which, in turn, increases the bending stiffness, and thus reduces deflection. This is the reasoning behind the first model. The main focus is to increase the bending stiffness in the radial direction, so the length of the pole-pieces is increased in the radial direction, as seen in Figure 5.2.

The deflection is assumed to decrease significantly in the radial direction, but less so in the tangential direction, since the stiffness only increases linearly with increasing pole-piece length. Next to that, it is expected that the torque will be reduced, due to the larger air gap, which will induce more leakage flux.

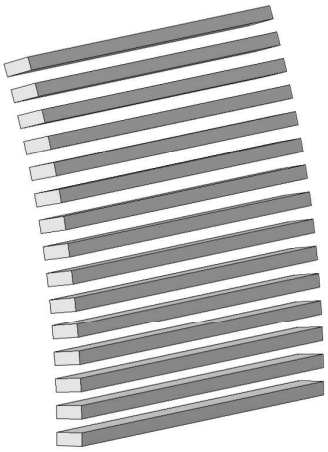

Figure 5.2: Geometry of the mechanical model with elongated pole-pieces

5.1.2 Bridged Pole-piece Rotor

With the second model, the aim is to reduce the deflection of the pole-pieces by connecting them together. Since the deflection of the separate pole-pieces is phase-shifted, it is expected that the deflection of the connected pole-pieces will be reduced. Taking the average over a

large number of connected pole-pieces, the phase shifts will compensate each other, reducing the deflection to a large extent.

This is also based on existing models widely used in existing literature [28, 29, 66–69]. However, in the current literature, the focus is only on the electromagnetic performance, and not the mechanical. Often, manufacturability and decreasing mechanical complexity is brought up as motivation to use this kind of mechanical model. Therefore, it is valuable to see whether these motivations make any sense, and whether the model can be applied to the INNWIND design as well. The model used in this report can be seen in Figure 5.3. It is assumed that the pole-pieces and the bridges between them are one piece made of the same material.

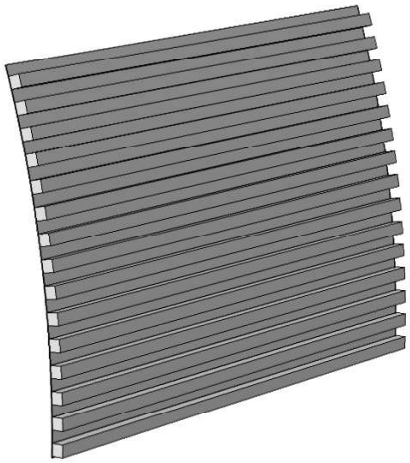

Figure 5.3: Geometry of the mechanical model with bridged pole-pieces

In this case, it is expected that the deflection in the tangential direction will almost disappear, and that the stiffness of the pole-pieces will be improved, making the array of pole-pieces one structure instead of an array of thin beams. However, due to the bridges, a lot of flux can leak from one magnetic pole to the other, without linking to the other permanent magnet array. This will increase the leakage flux and thus reduce the electromagnetic efficiency of the machine.

5.1.3 Ribbed Pole-piece Rotor

The third and last model is based on the previously discussed bridged pole-piece rotor. Instead of connecting the pole-pieces to each other along the length of the whole pole-pieces, they will be connected to each other in a one or a few specific location(s). These locations are based on the modal analysis done in Chapter 4, where it was discussed that the odd modes will cause the largest deflection. This means that the middle of the pole-pieces will always deflect the most, and thus, by connecting the pole-pieces there, deflection will be reduced, using the same reasoning used for the bridged pole-piece rotor. A possible configuration can be seen in Figure 5.4.

In this case, it is expected that the deflection will be decreased where the pole-pieces are connected. If the flux leakage is not too high, however, the torque of this model can be higher

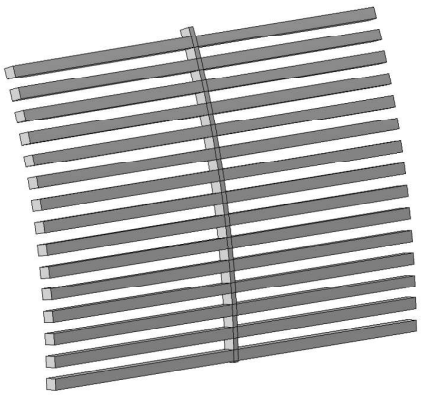

Figure 5.4: Geometry of the mechanical model with ribbed pole-pieces

than the bridged pole-piece rotor, since less of the magnetic flux is short-circuited through the bridges.

5.2 Improved Model Results

With the proposed models explained, the results can be presented. For each model, a simulation with a parametric sweep is done. This means that for every model, different cases or iterations are simulated, with every iteration having a slightly different pole-piece geometry. This is done to qualitatively discuss the improvement of the models over the original INNWIND design.

When this is done, the results are processed. Since the focus of this report is on the pole-piece deflection, this is the most important variable to evaluate. It is done by, for every iteration, taking the maximum deflection occurring at any time on any pole-piece. The result is one maximum deflection per iteration. Next tot that, the mechanical torque is evaluated as well. By doing this, the performance of the machine can be evaluated as well as the impact of changing the pole-pieces. The torque results from the electromagnetic model, which means there is one value per iteration. After each of these parameters have been processed, they are plotted against the change in the pole-piece geometry, giving a qualitative view on both the electromagnetic and mechanical performance of each model.

5.2.1 Elongated Pole-pieces

Elongating the pole-pieces is expected to primarily reduce the radial deflection due to the exponential increase in area moment of inertia shown by Equation 5.1. As can be seen in Figure 5.5, this is the general trend seen in the maximum deflection found in any pole-piece, ignoring the peak in the maximum radial deflection, which will be explained later. A line representing the air gap length is added to clearly show when the deflection exceeds the air gap length. It can be seen that doubling the height of the pole-pieces already reduces the deflection by almost 90 % to a maximum deflection of about 3.5 mm. It seems that the

minimum deflection of 1.3 mm is reached at a pole-piece height of 75 mm, after which the improvement stagnates.

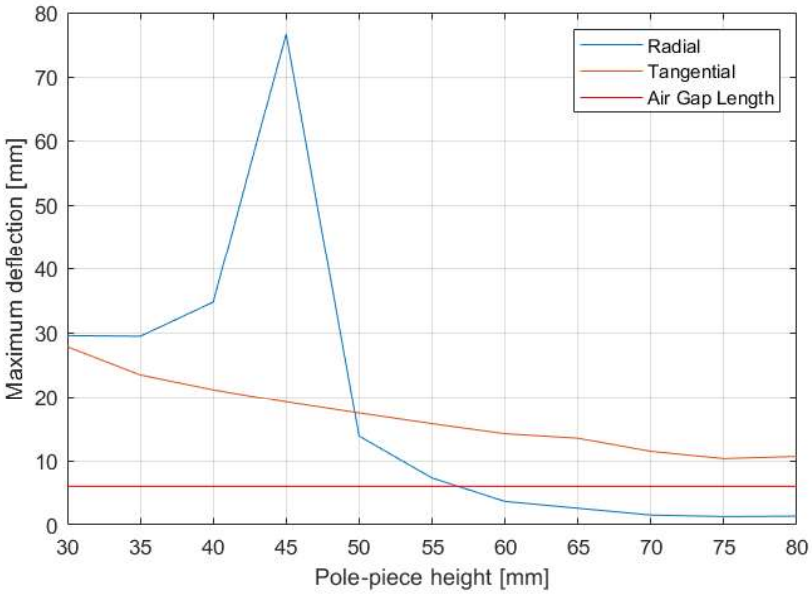

Figure 5.5: Maximum deflection of the pole-pieces versus pole-piece height

The reason why the deflection is still quite high is that it focuses on the deflection on the level of a single pole-piece, instead of using the out-of-phase deflection of near pole-pieces to balance the deflection out. This can be seen in Figure 5.6, where the deflection of two neighbouring pole-pieces is plotted. It can be seen that the deflection is out of phase, and connecting the pole-pieces could cancel out the individual deflection.

The peak seen in Figure 5.5 can be explained by the changing resonant frequency of the pole-pieces. In Equation 3.11, it can be seen that the resonance frequency is proportional to the area moment of inertia. This can also be observed in Figure 5.7, where the frequency spectrum of one of the pole-pieces is plotted. It can be seen that the higher the pole-pieces, the higher the resonance frequency becomes.

In Figure 5.8, the resonance frequency is plotted against the pole-piece height. An almost linear relation can be seen, which is to be expected from Equation 3.11. The resonance frequency and the pole-piece height should be exponentially proportional to the power of 1.5. However, at the scale seen in Figure 5.8, the relation becomes quasi linear.

The torque versus pole-piece height is shown in Figure 5.9, where an almost linear decrease of torque can be observed. At a pole-piece height of about 57 mm, where the deflection becomes lower than the air gap length, the torque decreases to about 8.3 MNm, which is a 12 % decrease in torque, and thus torque density. However, decreasing the deflection further to the minimum of 1.3 mm at a pole-piece height of 75 mm reduces the torque with another 7 % to about 7.7 MNm. The decreasing torque is mainly due to increased flux leakage. Since the pole-pieces are getting higher, so is the air gap as seen by the coils, as the high-speed rotor and its permanent magnet array move further away.

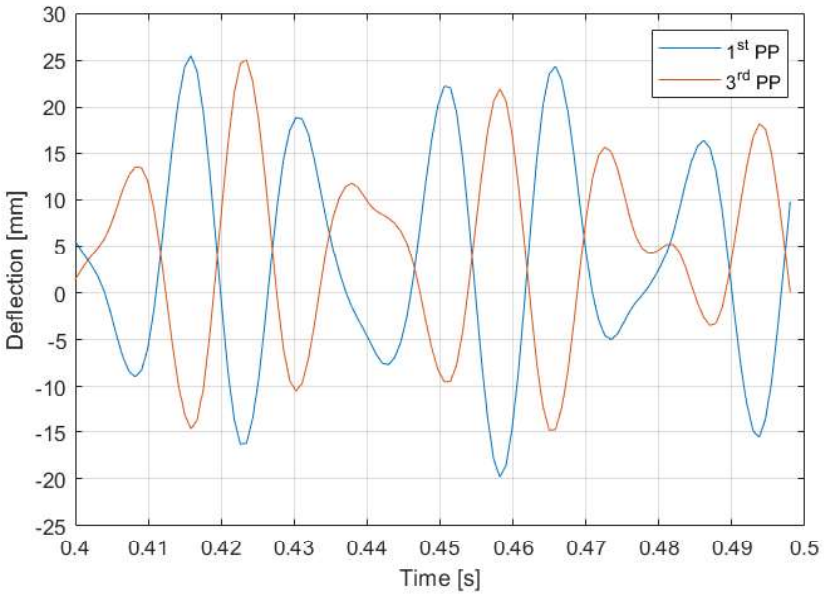

Figure 5.6: Radial deflection of two neighbouring pole-pieces of the elongated pole-piece model

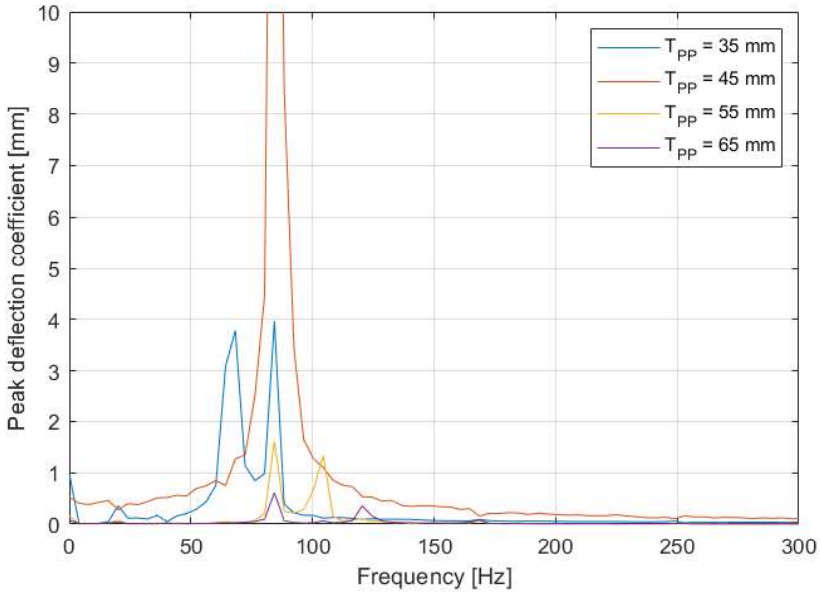

Figure 5.7: Frequency spectra of the pole-piece deflection for different pole-piece heights

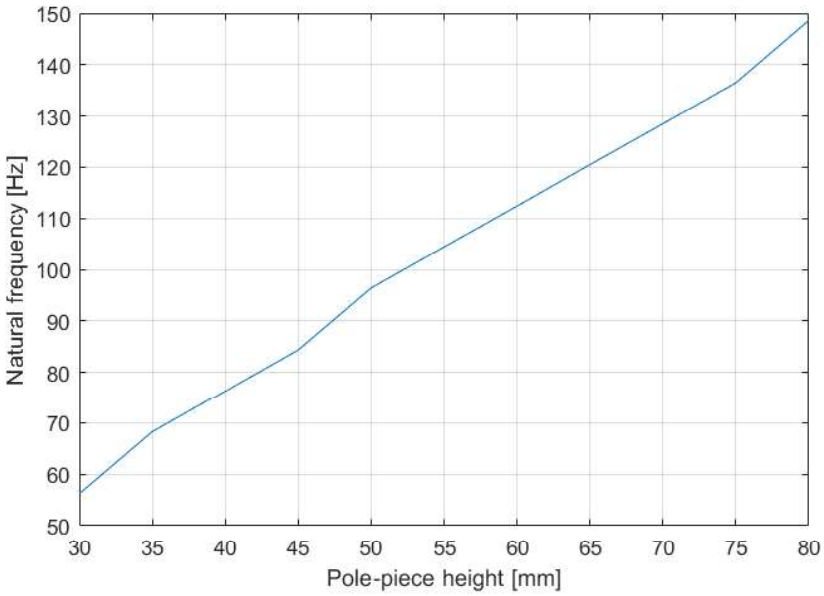

Figure 5.8: Pole-piece natural frequency versus pole-piece height

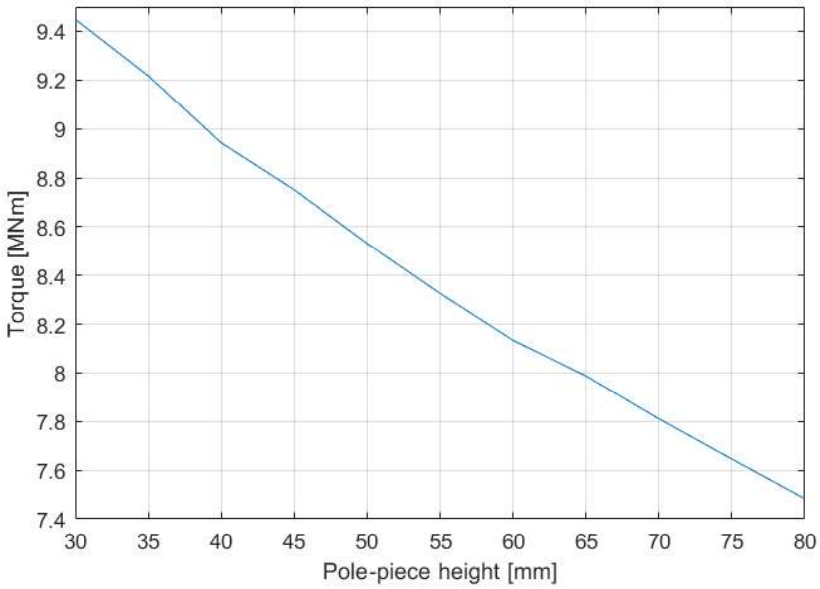

Figure 5.9: Torque versus pole-piece height

5.2.2 Bridged Pole-piece Rotor

The bridged pole-piece rotor is described in several articles [28, 29, 66–69], and its working principle is based on connecting the pole-pieces so they do not act like single thin beams any more, but as a closed cylinder with forces acting on the wall. This can be seen in Figure 5.10, where there is still some common-mode deflection, but the individual deflection is much less than a millimetre.

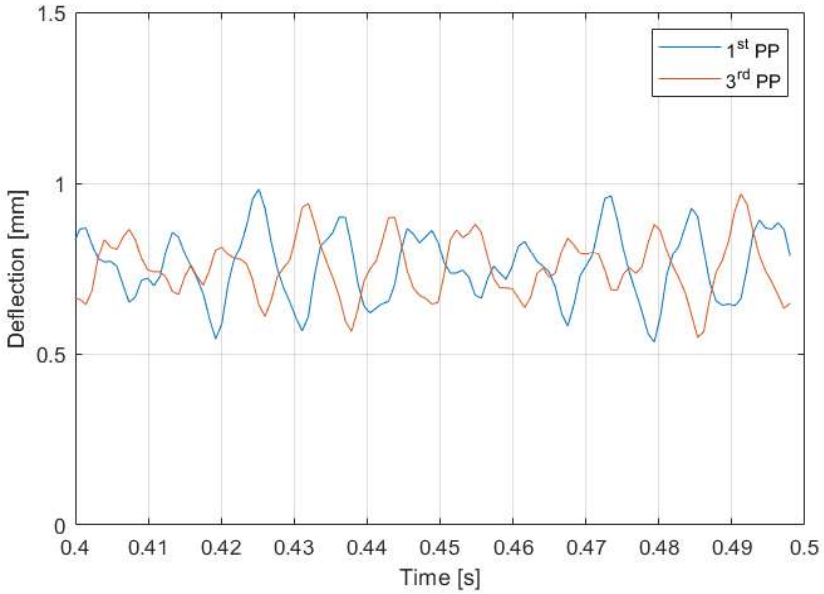

Figure 5.10: Radial deflection of two neighbouring pole-pieces for the bridged pole-piece model

Looking at the maximum deflection, from Figure 5.11, it can be seen that the maximum deflection is reduced drastically, already restricting the movement of the pole-pieces to almost 1 mm with even a 2 mm bridge between the pole-pieces. An exponential decrease can be seen with further increase in bridge thickness. The tangential deflection decreases linearly, starting from 0.2 mm with a 2 mm bridge thickness. This makes sense, as a linear increase in material linearly increases its resistance to normal stress.

The torque however decreases reasonably fast, decreasing from about 8 MNm at a bridge thickness of 2 mm, a drop of 15 % to about 2.7 MNm for a bridge thickness of 20 mm, a drop of 71 %. The big drop in torque is expected, as a bridge between the pole-pieces creates a low-reluctance magnetic path, and increases the flux leakage drastically. At 20 mm, the bridge is two thirds the size of the pole-pieces, approaching a case where the bridge is the same size as the pole-pieces. In that case, the pole-piece rotor is just a ring of steel, which short-circuits all magnetic circuits, and no torque is transferred any more.

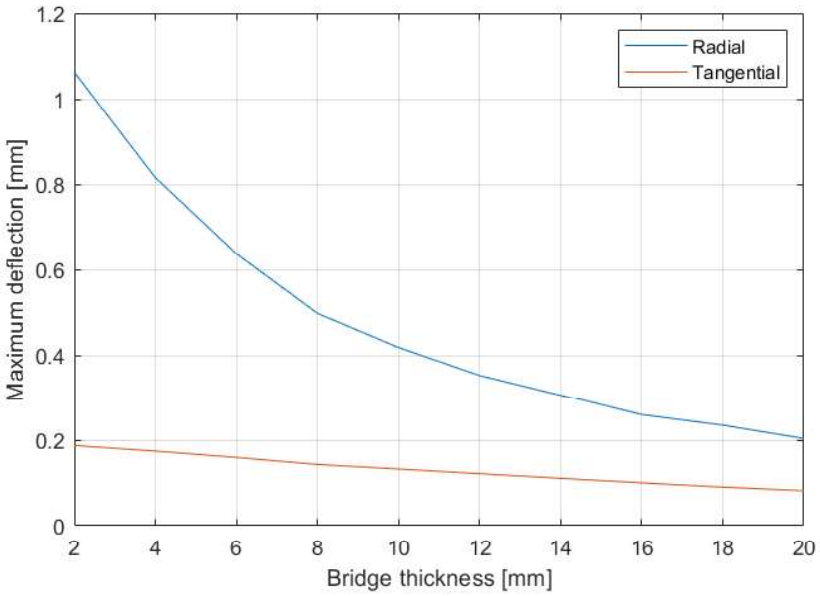

Figure 5.11: Maximum deflection of the pole-pieces versus bridge thickness

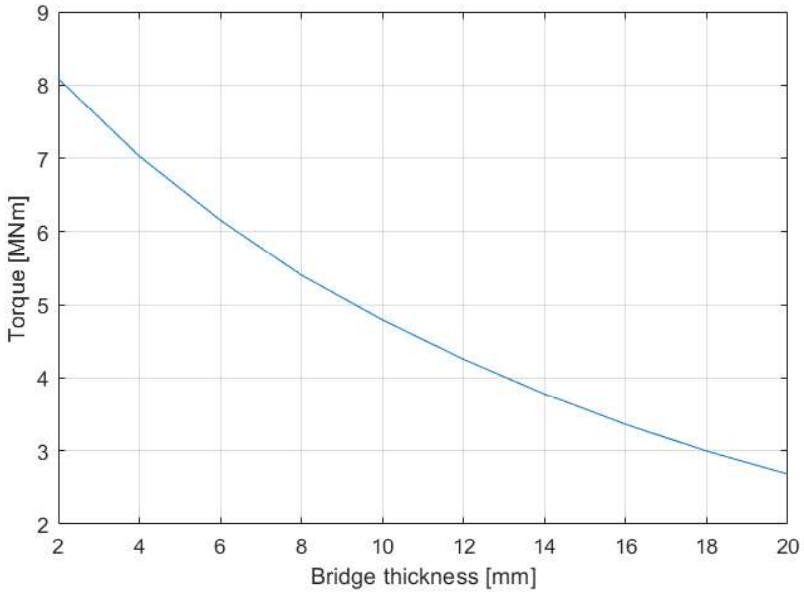

Figure 5.12: Torque versus bridge thickness

5.2.3 Ribbed Pole-piece Rotor

From the previous model, the bridged pole-pieces, it can be seen that having a bridge along the whole length of the pole-pieces causes a large drop in torque. The ribbed pole-piece rotor model tackles this problem by only connecting the pole-piece in one or a few spots. Only at those spots, the magnetic flux will be short-circuited. As with the bridged pole-piece rotor, most of the deflection is still from common-mode deflection, with individual deflection only being less than 0.1 mm.

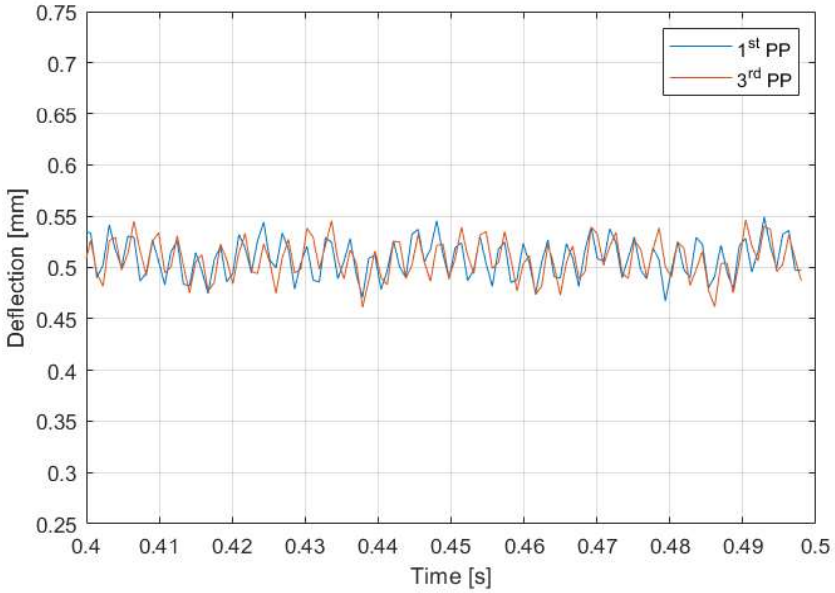

Figure 5.13: Radial deflection of two neighbouring pole-pieces for the ribbed pole-piece model

For this model, nine cases were simulated, changing two parameters: the number of ribs, from one to three , and the thickness of the rib(s), being 10, 30 and 50 mm. This results in three graphs for the radial direction, and three graphs for the tangential direction. These can be seen in Figure 5.14. It can be seen that the radial deflection decreases for increasing rib thickness, which is as expected. However, having two ribs does not seem to decrease the radial deflection at all. This can be explained using Figure 3.1, where it can be seen that when a beam is excited with a frequency around its first resonance frequency, the middle of the beam has the largest deflection. Having one or three ribs, spread evenly along the length of the beam, connects the pole-pieces in the middle. This means the point with the largest deflection is reinforced. In the case of only two evenly spread ribs, the middle is left disconnected, and thus left to deflect more compared to when there is a rib located in the middle.

The decrease in tangential deflection seems to largely come from an increase of ribs, while the thickness of the ribs does not decease the tangential deflection that much. This is a result of limiting the bending rotation of the pole-pieces. More ribs will limit the bending rotation at more locations, reducing the tangential deflection. Using a maximum deflection of one millimetre as the goal, it can be seen that either one rib of 45 mm, or three ribs of about 27

mm are needed. Looking at the tangential deflection, it can be seen that three ribs reduces the total deflection significantly more.

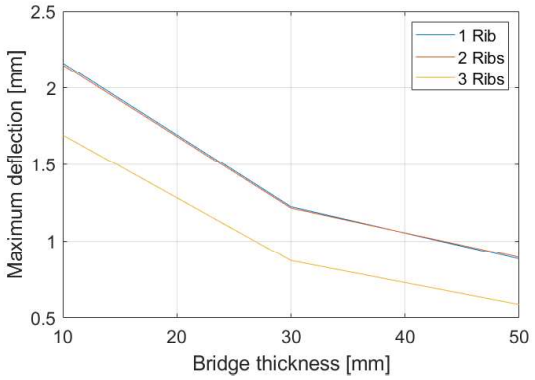

(a) Maximum radial deflection of the pole-pieces versus rib thickness for different numbers of ribs

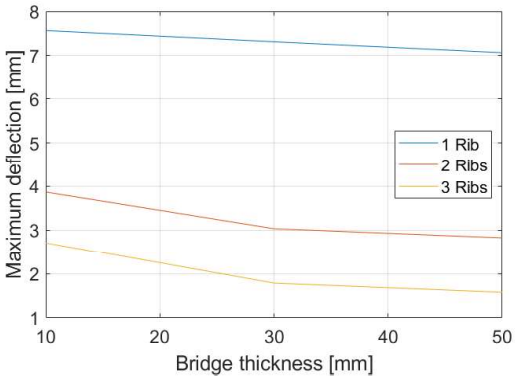

(b) Maximum tangential deflection of the pole-pieces versus rib thickness for different numbers ribs

Figure 5.14: Maximum deflection of the pole-pieces versus rib thickness

Due to the nature of this model, it is not possible to simulate the torque for any of these cases, as a three-dimensional electromagnetic model is needed to do this, which is not the scope of this project. However, it seems that this model can be quite promising considering only part of the pole-pieces is magnetically short-circuited.

Doing a solid mechanics simulation also results in plots showing the stress on the mechanical model, and the stress at the points where the pole-pieces are connected reaches values of about 2.3 MPa, which means it might also be possible to replace the steel connections by non-ferromagnetic ones which could be glued or welded to the pole-pieces. This way, the performance of the pole-pieces remains unchanged, while their deflection is drastically reduced. It could also be possible to have thinner bridges which will saturate, decreasing the flux leakage compared to the thick connections. More or wider connections would be needed though to limit the deflection, approaching a bridged pole-piece rotor model.

5.3 Comparing Results

Having discussed all three models, a rough comparison can be done. The goal is to keep the radial deflection under 1 mm. While this number is rather arbitrary at 1/6 of the air gap, it is chosen because the deflection is expected to be high due to the stronger magnetic fields. It is therefore unreasonable to choose a limit lower than 1 mm. This means that for each model, the changes needed to bring down the deflection as close as possible to 1 mm will be compared, as well as the decrease in torque, and thus torque density. This can be seen in Table 5-1.

Table 5-1: Overview of the modifications and their impact on the torque density

Model	Deflection	Modification	Torque decrease
Elongated pole-pieces	1.3 mm	75 mm high pole-pieces	19 %
Bridged pole-pieces	1 mm	2.5 mm thick bridges	17 %
Ribbed pole-pieces	1 mm	3 Ribs, 27 mm wide	-

It can be seen that the model with the elongated pole-pieces is unable to reach a deflection of less than 1 mm. On top of that, the decrease in torque is already 19 %, which is worse than the performance of the second model with the bridged pole-pieces. Next to that, the bridged pole-piece model reduces the tangential deflection drastically as well, with the elongated pole-piece model still having a tangential deflection of about 10 mm at a pole-piece height of 75 mm, whereas the tangential deflection of the bridged pole-pieces is less than 0.2 mm. However, a significant decrease in torque is still observed at 17 %.

The third model seems promising, reaching radial deflections of 1 mm and less relatively easily. However, due to the limitations of the model, nothing can be said about the decrease in torque due to the changed geometry or deflection. Since the pole-pieces are only magnetically short-circuited in a few places, it is possible that the decrease in torque is much less than 17 %, unless the edge effects become significant enough. This would mean the last model with the ribbed pole-piece rotor would be the best option to improve the mechanical performance of the INNWIND design.

Chapter 6

Conclusions and Recommendations

With all of the models made and results processed, this chapter will conclude the work done and results gathered and lessons learned in this report. The scientific contributions will be summarized, ending with recommendations which can guide future research on this topic.

6.1 Conclusions

In order to increase the share of wind energy generation, the LCOE should decrease, which is what projects like INNWIND focus on. This can be done by scaling up wind turbines and by increasing the reliability by using direct-drive generators. However, these tend to get very big and heavy, which is undesirable for offshore wind turbine installation. Magnetically geared machines, and specifically pseudo direct-drives where the magnetic gear and the direct-drive machine are incorporated within the same volume, have shown great promise to solve this problem. Pseudo direct-drives have shown to have superior torque densities compared to direct-drive machines, significantly reducing the size and weight of the machine. However, while there has been a lot of research on the electromagnetic performance of the pseudo direct-drive, no research has been done yet on the dynamic electromechanical performance of the pole-pieces, which was the focus of this thesis.

Because of the nature of the thesis, which revolved around numerical analysis, few analytical equations were used, with most results being extracted from numerical simulations. Due to its versatility, only one numerical tool was used: COMSOL Multiphysics, where all steps to be taken during numerical analysis can be done in the same user interface. Special care was taken in certain cases where COMSOL was not able to simulate the model correctly, such as balancing the high-speed rotor.

After setting up the simulation parameters correctly, the INNWIND pseudo-direct drive could be modelled. First, an electromagnetic model was made based on the geometry provided in the INNWIND report, followed by a simple mechanical model, consisting of steel beams ideally clamped at both ends. Both models were verified and showed great correspondence between either values given in the INNWIND report or calculated analytically.

Next, the results of the mechanical model could be extracted. It turns out that the total force on the pole-pieces reaches up to 24 kN, with the radial and tangential forces reaching up to 18 and 19 kN, respectively. This, in turn, causes a dynamical deflection of up to 31.2 mm in the radial direction, which is over five times the air gap length. This is due to the first resonance mode at 60.5 Hz, while the main frequency component of the electromagnetic force is at 83 Hz. This is close enough to cause resonance.

In order to reduce the deflection of the pole-pieces, three modifications to the pole-pieces are suggested. The first one relies on increasing the area moment of inertia of each individual pole-piece by increasing the pole-piece height. The other two rely on connecting the pole-pieces in order to mechanically reinforce them. The second model connects the pole-pieces with a thin bridge along the whole length of the pole-pieces, while the third only connects the pole-pieces with thicker connections at specific points.

It was shown that the deflection does decrease significantly if the pole-piece height is increased far enough to avoid the resonance frequency overlapping with the main frequency component of the electromagnetic force. However, the maximum radial deflection does not seem to get lower than 1.3 mm, which is still relatively high, while suffering from a large torque decrease.

The second model, where the pole-pieces are connected with a thin bridge along their whole length, is much more effective at decreasing the deflection of the pole-pieces, with a bridge of only 2 mm being enough to reduce the radial deflection to about 1 mm. However, a significant decrease in torque is observed as well due to the bridges short-circuiting the magnetic fields.

The third and last model also shows great promise, with the radial deflection limited to about 1 mm with three evenly spaced connections of about 27 mm. Unfortunately however, due to the limits of the model, nothing could be said about the electromagnetic performance of this model. So, while being very promising and only short-circuiting the magnetic fields, further research has to quantify how large the torque decrease is in order to be able to choose the most effective modification to the pole-piece rotor.

Although the results in this report are specific for the INNWIND design, it shows that attention should be paid to mechanical performance of the pole-pieces in order to guarantee the electromagnetic optimisation is valid. Due to the high magnetic flux density in the air gap and the long thin beams making up the pole-piece rotor, the deflection tends to be high as well, which means the mechanical requirements are also higher.

6.2 Contributions

The contributions of this thesis are threefold:

- It has been shown that the INNWIND design is not mechanically feasible. Deflections reach up to 31.2 mm whereas the air gap length is only 6 mm.
- Three simple modifications were suggested and quantitatively analysed to see how much they would reduce the mechanical deflection. Each of them showed to be able to reduce the deflection significantly.

- The three different modifications were qualitatively compared in order to decide which is the most promising modification to be used in further designs. While some data is missing, a promising modification is identified, next to showing that the bridged topology, which is widely used in literature, is a very good option.

6.3 Recommendations

While the research done in this report already shows useful results, a lot more can be done to improve the accuracy of the results and to allow for more efficient future research. Four main domains of improvement can be identified:

- A lot of data is missing on the mechanical model, such as how the pole-pieces are attached to the pole-piece rotor flanges and how structurally sound the whole rotor is. In this report, it is assumed the pole-piece ends are fixed and cannot rotate or move. In reality, a slight rotation of the ends might result in a large increase in deflection in the middle of the pole-piece. Doing a electromechanical analysis of the whole pole-piece rotor including flanges would result in more accurate results.
- In order to reduce the computational resources spent, especially when including rotor flanges, it would be advantageous to analyse the mechanical performance using modal analysis. This could save time by only calculating the response to frequency components present in the applied load. Doing an inverse FFT would then result in time domain results of the deflection of the model. This would also require mechanical verification compatible with modal analysis.
- Another idealisation used in this report is one-way coupled analysis. This way of modelling could be accurate enough when the mechanical deflections are small, but as shown in this report, the deflections are considerable. This means that in order to get more accurate results, a two-way coupled analysis should be implemented. Because the deflection of the pole-pieces is not uniform along its length, a three-dimensional electromagnetic model would be needed as well. Next to being able to implement a two-way coupled analysis, it would also allow for taking into account edge effects of the electromagnetic model.
- Lastly, the scope of the model is the mechanical deflection of the pole-pieces versus the pole-piece rotor torque. However, another interesting metric to trade off the decreased deflection would be machine efficiency. In order to be able to say something about the efficiency of the model, a loss model would need to be included. This could be an analytical one, or could be implemented in the numerical model.

Bibliography

[1] "The Paris Agreement | UNFCCC," Dec. 2015.

[2] "Limiting Global Climate Change to 2 degrees Celsius. The way ahead for 2020 and beyond." Commision of the European Communities, Brussels, Tech. Rep., Jan. 2007.

[3] "Trends and projections in Europe 2018 - Tracking progress towards Europe's climate and energy targets — European Environment Agency." [Online]. Available: https://www.eea.europa.eu/publications/trends-and-projections-in-europe-2018-climate-and-energy

[4] "Wind energy in Europe: Outlook to 2023 | WindEurope." [Online]. Available: https://windeurope.org/about-wind/reports/wind-energy-in-europe-outlook-to-2023/

[5] "GWEC Global Wind Report," Apr. 2018.

[6] "The European Power Sector in 2017. State of Affairs and Review of Current Developments," Jan. 2018.

[7] M. van Benthem and B. Tieben, "Zeewind versus kolenstroom," seo economisch onderzoek, Amsterdam, Tech. Rep., Jun. 2017.

[8] "Making green energy affordable," Ørsted, Gentofte, Denmark, Tech. Rep., Jun. 2019.

[9] "Renewable power generation costs in 2017," p. 160, Jan. 2018.

[10] "Offshore Wind Outlook 2019: World Energy Outlook Special Report," *Offshore Wind*, Oct. 2019.

[11] "LCOE reduction for the next generation offshore wind turbines," Oct. 2017.

[12] P. Chaviaropoulos and A. Natarajan, "Definition of PIs and Target Values," Tech. Rep., Feb. 2014.

[13] J. M. Pinar Perez, F. P. Garcia Marquez, A. Tobias, and M. Papaelias, "Wind turbine reliability analysis," *Renewable and Sustainable Energy Reviews*, vol. 23, pp. 463–472, Jul. 2013. [Online]. Available: https://linkinghub.elsevier.com/retrieve/pii/S1364032113001779

[14] M. Shafiee and F. Dinmohammadi, "An FMEA-Based Risk Assessment Approach for Wind Turbine Systems: A Comparative Study of Onshore and Offshore," *Energies*, vol. 7, no. 2, pp. 619–642, Feb. 2014. [Online]. Available: http://www.mdpi.com/1996-1073/7/2/619

[15] U. Shipurkar, "Improving the Availability of Wind Turbine Generator Systems," Ph.D. dissertation, TU Delft, 2019.

[16] G. Shrestha, "Structural flexibility of large direct drive generators for wind turbines." Ph.D. dissertation, [s.n.], S.l., 2013, oCLC: 905869649.

[17] Y. Wang, M. Filippini, N. Bianchi, and P. Alotto, "A Review on Magnetic Gears: Topologies, Computational Models and Design Aspects," in *2018 XIII International Conference on Electrical Machines (ICEM)*, Sep. 2018, pp. 527–533.

[18] P. M. Tlali, R.-J. Wang, and S. Gerber, "Magnetic gear technologies: A review," in *2014 International Conference on Electrical Machines (ICEM)*. Berlin, Germany: IEEE, Sep. 2014, pp. 544–550. [Online]. Available: http://ieeexplore.ieee.org/document/6960233/

[19] P. Rasmussen, T. Andersen, F. Joergensen, and O. Nielsen, "Development of a high performance magnetic gear," in *38th IAS Annual Meeting on Conference Record of the Industry Applications Conference, 2003.*, vol. 3. Salt Lake City, UT, USA: IEEE, 2003, pp. 1696–1702. [Online]. Available: http://ieeexplore.ieee.org/document/1257784/

[20] A. Penzkofer and K. Atallah, "Magnetic Gears for High Torque Applications," *IEEE Transactions on Magnetics*, vol. 50, no. 11, pp. 1–4, Nov. 2014.

[21] K. Atallah, J. Rens, S. Mezani, and D. Howe, "A Novel "Pseudo" Direct-Drive Brushless Permanent Magnet Machine," *IEEE Transactions on Magnetics*, vol. 44, no. 11, pp. 4349–4352, Nov. 2008. [Online]. Available: http://ieeexplore.ieee.org/document/4717785/

[22] R. Qu, D. Li, and J. Wang, "Relationship between magnetic gears and vernier machines," in *2011 International Conference on Electrical Machines and Systems*. Beijing, China: IEEE, Aug. 2011, pp. 1–6. [Online]. Available: http://ieeexplore.ieee.org/document/6073448/

[23] P. O. Rasmussen, T. V. Frandsen, K. K. Jensen, and K. Jessen, "Experimental Evaluation of a Motor-Integrated Permanent-Magnet Gear," *IEEE Transactions on Industry Applications*, vol. 49, no. 2, pp. 850–859, Mar. 2013.

[24] A. B. Abrahamsen, D. Liu, and H. Polinder, "Final assessment of superconducting and pseudo direct-drive generator performance indicators," Oct. 2017.

[25] L. N. Jian, K. T. Chau, D. Zhang, J. Z. Jiang, and Z. Wang, "A Magnetic-Geared Outer-Rotor Permanent-Magnet Brushless Machine for Wind Power Generation," *IEEE TRANSACTIONS ON INDUSTRY APPLICATIONS*, p. 8, 2007.

[26] A. Penzkofer, "Analytical Modelling and Analysis of Magnetic Gears and Pseudo Direct Drives for Large Wind Turbines," Ph.D. dissertation, The University Of Sheffield, 2016.

[27] X. Zhang, "Design and Analysis of Magnetic-geared Transmission Devices for Low-speed Hightorque Applications," Ph.D. dissertation, Aalborg University, Aug. 2017.

[28] D. Z. Abdelhamid and A. M. Knight, "The Effect of Modulating Ring Design on Magnetic Gear Torque," *IEEE Transactions on Magnetics*, vol. 53, no. 11, pp. 1–4, Nov. 2017.

[29] K. K. Uppalapati, J. Kadel, J. Wright, K. Li, W. Williams, and J. Z. Bird, "A low assembly cost coaxial magnetic gearbox," in *2016 IEEE 2nd Annual Southern Power Electronics Conference (SPEC)*, Dec. 2016, pp. 1–6.

[30] M. Desvaux, "Optimisation mecatronique de multiplicateurs magnetiques pour le grand eolien," Ph.D. dissertation, Université Bretagne Loire, Jul. 2018.

[31] A. Penzkofer and K. Atallah, "Design and PI of PDD generator," Aug. 2015.

[32] M. Desvaux, H. Bildstein, B. Multon, H. B. Ahmed, S. Sire, A. Fasquelle, and D. Laloy, "Magnetic losses and thermal analysis in a magnetic gear for wind turbine," in *2018 Thirteenth International Conference on Ecological Vehicles and Renewable Energies (EVER)*, Apr. 2018, pp. 1–7.

[33] A. Belahcen, "Magnetoelastic coupling in rotating electrical machines," *IEEE Transactions on Magnetics*, vol. 41, no. 5, pp. 1624–1627, May 2005.

[34] ——, "Vibrations of rotating electrical machines due to magnetomechanical coupling and magnetostriction," *IEEE Transactions on Magnetics*, vol. 42, no. 4, pp. 971–974, Apr. 2006.

[35] M. Kirschneck, D. J. Rixen, H. Polinder, and R. A. J. van Ostayen, "Electromagnetomechanical Coupled Vibration Analysis of a Direct-Drive Off-Shore Wind Turbine Generator," *Journal of Computational and Nonlinear Dynamics*, vol. 10, no. 4, p. 041011, Jul. 2015. [Online]. Available: http://computationalnonlinear.asmedigitalcollection.asme.org/article.aspx?doi=10.1115/1.4027837

[36] M. Cheraghi, M. Karimi, and M. B. Booin, "An investigation on acoustic noise emitted by induction motors due to magnetic sources," in *2018 9th Annual Power Electronics, Drives Systems and Technologies Conference (PEDSTC)*, Feb. 2018, pp. 104–109.

[37] M. Kirschneck, D. J. Rixen, H. Polinder, and R. A. J. van Ostayen, "Effects of Magneto-Mechanical Coupling on Structural Modal Parameters," in *Topics in Modal Analysis II, Volume 8*, ser. Conference Proceedings of the Society for Experimental Mechanics Series, R. Allemang, Ed. Springer International Publishing, 2014, pp. 11–18.

[38] C. G. Armstrong, T. D. B. Carse, and P.-T. M. Device, "UNITED STATES PATENT OFFICE." p. 4, 1901.

[39] H. T. Faus, "Magnet gearing," US Patent US2 243 555A, May, 1941. [Online]. Available: https://patents.google.com/patent/US2243555A/en?oq=US2243555A

[40] J. D. Livingston, "The history of permanent-magnet materials," *JOM*, vol. 42, no. 2, pp. 30–34, Feb. 1990. [Online]. Available: https://doi.org/10.1007/BF03220870

[41] T. Kuno, S. Suzuki, K. Urushibata, K. Kobayashi, N. Sakuma, M. Yano, A. Kato, and A. Manabe, "(Sm,Zr)(Fe,Co)11.0-11.5ti1.0-0.5 compounds as new permanent magnet materials," *AIP Advances*, vol. 6, no. 2, p. 025221, Feb. 2016. [Online]. Available: https://aip.scitation.org/doi/full/10.1063/1.4943051

[42] G. Bai, R. W. Gao, Y. Sun, G. B. Han, and B. Wang, "Study of high-coercivity sintered NdFeB magnets," *Journal of Magnetism and Magnetic Materials*, vol. 308, no. 1, pp. 20–23, Jan. 2007. [Online]. Available: http://www.sciencedirect.com/science/article/pii/S030488530600775X

[43] J. T. B. Martin, "Magnetic transmission," US Patent US3 378 710A, Apr., 1968. [Online]. Available: https://patents.google.com/patent/US3378710A/en

[44] N. Laing, "Magnetic transmission," US Patent US3 645 650A, Feb., 1972. [Online]. Available: https://patents.google.com/patent/US3645650A/en

[45] R. Hornreich and S. Shtrikman, "Optimal design of synchronous torque couplers," *IEEE Transactions on Magnetics*, vol. 14, no. 5, pp. 800–802, Sep. 1978.

[46] K. Atallah and D. Howe, "A novel high-performance magnetic gear," *IEEE Transactions on Magnetics*, vol. 37, no. 4, pp. 2844–2846, Jul. 2001.

[47] K. Atallah, S. D. Calverley, and D. Howe, "Design, analysis and realisation of a high-performance magnetic gear," *IEE Proceedings - Electric Power Applications*, vol. 151, no. 2, pp. 135–143, Mar. 2004.

[48] M. Venturini and F. Leonardi, "High torque, low speed joint actuator based on PM brushless motor and magnetic gearing," in *Conference Record of the 1993 IEEE Industry Applications Conference Twenty-Eighth IAS Annual Meeting*, Oct. 1993, pp. 37–42 vol.1.

[49] A. G. Razzell and J. J. A. Cullen, "Compact electrical machine," US Patent US6 794 781B2, Sep., 2004. [Online]. Available: https://patents.google.com/patent/US6794781B2/en

[50] K. Atallah, S. Calverley, R. Clark, J. Rens, and D. Howe, "A new PM machine topology for low-speed, high-torque drives," in *2008 18th International Conference on Electrical Machines*, Sep. 2008, pp. 1–4.

[51] A. Fitzgerald, C. J. Kingsley, and S. Umans, *Fitzgerald & Kingsley's Electric Machinery*, 7th ed. New York, NY: McGraw-Hill, 2014.

[52] "Analysis of Deformation in Solid Mechanics." [Online]. Available: https://www.comsol.com/multiphysics/analysis-of-deformation

[53] "What Is Structural Mechanics? - An Introductory Guide." [Online]. Available: https://www.comsol.com/multiphysics/introduction-to-structural-mechanics

[54] "Why All These Stresses and Strains?" [Online]. Available: https://www.comsol.com/blogs/why-all-these-stresses-and-strains/

[55] R. G. Budynas and J. K. Nisbett, *Shigley's Mechanical Engineering Design*, 10th ed. New York: McGraw-Hill, 2015.

[56] F. P. Beer, Ed., *Mechanics of materials*, 6th ed. New York: McGraw-Hill, 2011.

[57] M. Nakao, "Collapse of Tacoma Narrows Bridge," p. 6.

[58] W. T. Thomson, *Theory of Vibration with Applications*, 4th ed.

[59] C. M. Harris and A. G. Piersol, Eds., *Harris' shock and vibration handbook*, 5th ed., ser. McGraw-Hill handbooks. New York: McGraw-Hill, 2002.

[60] "Solutions to Linear Systems of Equations: Direct and Iterative Solvers | COMSOL Blog." [Online]. Available: https://www.comsol.com/blogs/solutions-linear-systems-equations-direct-iterative-solvers/

[61] "Understanding the Fully Coupled vs. Segregated approach and Direct vs. Iterative linear solvers - 1258 - Knowledge Base." [Online]. Available: https://www.comsol.com/support/knowledgebase/1258/

[62] A. Arkkio, *Analysis of induction motors based on the numerical solution of the magnetic field and circuit equations*. Helsinki University of Technology, Dec. 1987. [Online]. Available: https://aaltodoc.aalto.fi:443/handle/123456789/2158

[63] S. Sgobba, "Physics and measurements of magnetic materials," p. 25.

[64] R. W. De Doncker, D. W. J. Pulle, and A. Veltman, *Advanced electrical drives: analysis, modeling, control*, ser. Power systems. Dordrecht: Springer, 2011, oCLC: 731692732.

[65] L. Hanzo, M. El-Hawary, B.-M. Hammerli, M. Lanzerotti, D. Jacobson, O. P. Malik, S. Nahavandi, T. Samad, G. Zobrist, and K. Moore, *POWER CONVERSION AND CONTROL OF WIND ENERGY SYSTEMS*. John Wiley & Sons, Inc., 2011.

[66] D.-K. Jang and J.-H. Chang, "Effect of Stationary Pole Pieces with Bridges on Electromagnetic and Mechanical Performance of a Coaxial Magnetic Gear," *Journal of Magnetics*, vol. 18, no. 2, pp. 207–211, 2013. [Online]. Available: http://www.koreascience.or.kr/article/JAKO201318449151705.page

[67] T. Fujita, Y. Ando, K. Nagaya, M. Oka, T. Todaka, M. Enokizono, and K. Sugiura, "Surface Magnet Gears with a New Magnet Arrangement and Optimal Shape of Stationary Pole Pieces," *Journal of Electromagnetic Analysis and Applications*, vol. 05, no. 06, pp. 243–249, 2013. [Online]. Available: http://www.scirp.org/journal/doi.aspx?DOI=10.4236/jemaa.2013.56039

[68] B. Ackermann and L. Honds, "Magnetic drive arrangement comprising a plurality of magnetically cooperating parts which are movable relative to one another," US Patent US5 633 555A, May, 1997. [Online]. Available: https://patents.google.com/patent/US5633555A/en

[69] N. W. Frank and H. A. Toliyat, "Analysis of the Concentric Planetary Magnetic Gear With Strengthened Stator and Interior Permanent Magnet Inner Rotor," *IEEE Transactions on Industry Applications*, vol. 47, no. 4, pp. 1652–1660, Jul. 2011.